



Examining the consistency of products derived from various ocean color sensors in open ocean (Case 1) waters in the perspective of a multi-sensor approach

André Morel ^{a,*}, Yannick Huot ^a, Bernard Gentili ^a, P. Jeremy Werdell ^b,
Stanford B. Hooker ^b, Bryan A. Franz ^b

^a *Laboratoire d'Océanographie de Villefranche (CNRS and Université P & M Curie) BP 08 06238 Villefranche-sur-mer, France*

^b *NASA Goddard Space Flight Center, Greenbelt, Maryland, USA*

Received 13 November 2006; received in revised form 26 March 2007; accepted 27 March 2007

Abstract

During its lifetime, a space-borne ocean color sensor provides world-wide information about important biogeochemical properties of the upper ocean every 2 to 4 days in cloudless regions. Merging simultaneous or complementary data from such sensors to obtain better spatial and temporal coverage is a recurring objective, but it can only be reached if the consistency of the sensor-specific products, as delivered by the various Space Agencies, has first been carefully examined. The goal of the present study is to provide a procedure for establishing a coherency of open ocean (Case-1 waters) data products, for which the various data processing methods are sufficiently similar. The development of the procedure includes a detailed comparison of the marine algorithms used (after atmospheric corrections) by space agencies for the production of standard products, such as the chlorophyll concentration, [Chl], and the diffuse attenuation coefficient, K_d . The MODIS-Aqua, SeaWiFS and MERIS [Chl] products agree over a wide range, between ~ 0.1 and 3 mg m^{-3} , whereas increasing divergences occur for oligotrophic waters ([Chl] (from 0.02 to 0.09 mg m^{-3}). For the $K_d(490)$ coefficient, different algorithms are in use, with differing results. Based on a semi-analytical reflectance model and hyperspectral approach, the present work proposes a harmonization of the algorithms allowing the products of the various sensors to be comparable, and ultimately, meaningfully merged (the merging procedures themselves are not examined). Additional potential products, obtained by using [Chl] as an intermediate tool, are also examined and proposed. These products include the thickness of the layer heated by the sun, the depth of the euphotic zone, and the Secchi disk depth. The physical limitations in the predictive skill of such downward extrapolations, made from information concerning only the upper layer, are stressed.

© 2007 Elsevier Inc. All rights reserved.

Keywords: Ocean color sensors; Chlorophyll; Attenuation coefficient; Multi-sensor products; Products consistency; Heated layer; Euphotic layer; Secchi disk; Merging

1. Introduction

From the perspective of merging data stream delivered by different space-borne ocean color sensors, as advocated by SIMBIOS (1999), and IOCCG (2004) (see list of acronyms, Appendix A), it is necessary to verify that the products to be merged are defined and computed in the same, or at least in compatible, ways. The normalized water-leaving radiance, nLw, or similar quantities, as remote sensing reflectance, R_{rs} , and

irradiance reflectance, R (Definitions in Appendix B) are well defined radiometric quantities, and their exact definitions are shared by the cognizant space agencies. This does not mean that the actual products of these agencies are strictly equal or numerically interconvertible. Indeed, uncertainties in calibration (affecting the quantification of the initial signal recorded at the top-of-atmosphere level), then differences in the atmospheric correction schemes (affecting the magnitude of the retrieved marine signals) may introduce some distortions. Such potential divergences are beyond the scope of the present study. In what follows, it will be assumed that these discrepancies or biases, if any, are identified or under control. In such a case, the nLw (or

* Corresponding author.

E-mail address: morel@obs-vlfr.fr (A. Morel).

similar quantities) from differing data sources are assumed to be consistent within their own uncertainty levels, so that any data merging (including a bias-correcting procedure) can be meaningfully attempted. Note that the merging techniques are out of the scope of the present study; its primary objective is to examine the consistency of two main geophysical products which are derived from the marine signals (supposed to be accurately retrieved).

Specifically, the focus will be on the phytoplankton concentration (or pigment index), generally expressed as chlorophyll concentration (mg m^{-3}), thereafter denoted by $[\text{Chl}]$, and on the diffuse attenuation for downward irradiance, K_d (m^{-1}), at a given wavelength (e.g. at 490 nm). These products are computed using algorithms which manipulate, in various manners, the radiometric spectral signals as retrieved at the sea level. Most of these algorithms (in particular those examined here) have been established for, and are only pertinent to, Case-1 waters. For historical reasons, however, (in particular because of the use of differing channel combinations, distinct scientific approaches, as well as independent field data bases), these algorithms differ to an extent which deserves examination. The ocean color algorithms considered here are those which are the operationally validated algorithms, in use with SeaWiFS, MODIS-Aqua (MODIS-A), and MERIS (next re-processing), and routinely providing global products. As a complementary objective, the possibility of using $[\text{Chl}]$ and K_d for tentative predictions of the heat deposition, the euphotic layer depth, and the Secchi disk depth are also examined.

It is worth noting that the derivation of other products, not restricted to Case-1 waters, is presently under investigation (see e.g., IOCCG, 2000, 2006; Lee et al., 2002, 2005; Loisel et al., 2002; Maritorena et al., 2002). These on-going studies aim at retrieving additional geophysical products, such as the concentrations of colored dissolved organic matter and of suspended sediments, or some inherent optical properties of the water body, such as the absorption and the backscattering coefficients. They are at the root of bio-optical model-based merging techniques (Maritorena & Siegel, 2005). These new products and various proposed methodologies are out of the scope of the present study, which is restricted to the examination of the coherency of the data streams, as they are routinely produced by satellite missions.

2. Pigment algorithms

To derive the phytoplankton pigment concentration, Morel and Gordon (1980) described a purely empirical, a semi-analytical, and an analytical approach. The latter still remains somewhat elusive (discussion in Morel & Maritorena, 2001, thereafter denoted by MM01). Only the empirical approach (SeaWiFS and MODIS-A) and the semi-analytical approach (for MERIS) are employed on a routine basis. Before these algorithms are compared, their typical features are briefly summarized.

2.1. First approach

The *purely empirical* approach was originally developed in view of processing the global CZCS dataset (Clark, 1981). It

was then refined using an increased number of simultaneous field observations of $[\text{Chl}]$ and remote sensing reflectance, $R_{rs}(\lambda)$, at several specific wavelengths (λ) (assembled by the NASA SeaWiFS Bio-optical Archive and Storage System, SeaBASS, Hooker et al., 1994; Werdell & Bailey, 2002). The coherent and consolidated dataset assembled by the SeaBAM group (O'Reilly et al., 2000) was statistically analyzed in view of developing the ocean chlorophyll 2-band, 3-band, and 4-band algorithms OC2, OC3, and OC4 (O'Reilly et al., 1998, updated in O'Reilly et al., 2000). In essence, these algorithms are obtained as being the best fit when relating the log-transform of the observed $[\text{Chl}]$ and the log-transform of the R_{rs} ratios; these quantities (also called blue-to-green ratios) are the ratios $R_{rs}(\lambda_i)/R_{rs}(\lambda_j)$, denoted by $^iR_{rs}$, of observed remote sensing reflectance at two wavelengths, namely at a wavelength in the green domain of the spectrum ($\lambda_j \sim 550\text{--}560$ nm), and at one of three available λ , in the blue and blue-green domain (namely $\lambda_i \sim 443$, ~ 490 and ~ 510 nm).

The OC2 algorithm only uses the single $R_{rs}(490)/R_{rs}(555)$ ratio. The OC3 algorithm, employed by MODIS-A, uses the largest of the $R_{rs}(443)/R_{rs}(551)$, and $R_{rs}(488)/R_{rs}(551)$ ratios, while OC4 (SeaWiFS) uses in the same way the largest of the three, $R_{rs}(443)/R_{rs}(555)$, $R_{rs}(490)/R_{rs}(555)$, and $R_{rs}(510)/R_{rs}(555)$ ratios. Because the statistical relationships (then used as algorithms) were obtained in log-log space, and their best functional representation is achieved through polynomials, their general structure is

$$\log_{10}[\text{Chl}] = a_0 + \sum_{n=1}^N a_n [\log_{10}(^iR_{rs})]^n \quad (1)$$

where $N=4$ for OC3 and OC4 algorithms, and $N=3$ for OC2 (no longer routinely used). The identifiers of the various algorithms are provided in Table 1. The operational algorithms for SeaWiFS (OC4V4) and for MODIS-A (OC3M) are graphically shown (Fig. 1).

2.2. Second approach

The *semi-analytical* approach rests on the introduction of spectral inherent optical properties, namely the absorption coefficient, $a(\lambda)$, and the backscattering coefficient, $b_b(\lambda)$ into a simplified solution of the radiative transfer equation; through this solution, the irradiance reflectance, $R(\lambda)$ (definition in Appendix B) is an explicit function of these inherent coefficients (Gordon et al., 1975; Morel & Prieur, 1977), such as (λ omitted)

$$R = f[b_b/a] \quad (2)$$

or

$$R = f'[b_b/(a + b_b)] \quad (2')$$

where f and f' , the spectrally-dependent dimensionless factors, depend on the incident radiance field (determined by the solar zenith angle, and the atmospheric properties). These factors also depend on the optical properties of the water body (Morel

Table 1
Algorithms: identifiers and structure

Y represents the derived variable

General structure:

$$\log_{10}[Y] = a_0 + \sum_1^N a_n [\log_{10}(^iR_{rs} \text{ or } R_j^i)]^n$$

Identifier	Y	Band ratio and specific form
<i>SeaWiFS and MODIS Algorithms (NASA)</i>		
OC4v4	[Chl]	$^iR_{rs} = \max(^{443}_{555}R_{rs}, ^{490}_{555}R_{rs}, ^{510}_{555}R_{rs})$
OC3Mo	[Chl]	$^iR_{rs} = \max(^{443}_{555}R_{rs}, ^{490}_{555}R_{rs})$
OC2v4	[Chl]	$^iR_{rs} = ^{490}_{555}R_{rs}$
<i>MERIS Algorithm (ESA)</i>		
OC4Me ^a	[Chl]	$R_j^i = \max(R_{560}^{443}, R_{560}^{490}, R_{560}^{510})$
<i>MERIS type algorithms^b</i>		
OC4Me555	[Chl]	$^iR_{rs} = \max(^{443}_{555}R_{rs}, ^{490}_{555}R_{rs}, ^{510}_{555}R_{rs})$
OC3Me550	[Chl]	$^iR_{rs} = \max(^{443}_{555}R_{rs}, ^{490}_{555}R_{rs})$
OC2Me560	[Chl]	$^iR_{rs} = ^{490}_{560}R_{rs}$
OC2Me555	[Chl]	$^iR_{rs} = ^{490}_{555}R_{rs}$
<i>K_d algorithms</i>		
OK2-555	$K_{bio}(490)$	$^iR_{rs} = ^{490}_{555}R_{rs}$
OK2-550	$K_{bio}(490)$	$^iR_{rs} = ^{490}_{550}R_{rs}$
OK2-560 ^a	$K_{bio}(490)$	$R_j^i = R_{560}^{490}$

then $K_d(490) = 0.0166 + K_{bio}(490)$

Conventions: the denominations OC and OK are used for algorithms providing [Chl] and K_d , respectively; the suffixes “M” and “Me” stand for MODIS and MERIS algorithms; when needed, the green reference wavelengths (550, 555, 560 nm) are added; “v” inside an acronym means “version”; $^iR_{rs}$ represents a ratio of remote sensing reflectance (R_{rs}) at the two wavelengths i and j .

R_j^i represents a ratio of irradiance reflectance (R) at the two wavelengths i and j .

^a For MERIS (based on irradiance reflectance ratios).

^b Both versions using either $^iR_{rs}$ or R_j^i are available.

In Gordon et al. (1988), the absorption coefficient, $a(\lambda, \text{Chl})$, was replaced by a surrogate, the diffuse attenuation coefficient for downward irradiance, $K_d(\lambda, \text{Chl})$, and this coefficient was related to [Chl] in Case-1 waters according to the formulation of Baker and Smith (1982). The f^* factor was modified accordingly to account for the use of K_d instead of a in Eq. (2'). In contrast, Morel (1988) iteratively derived $a(\lambda, \text{Chl})$ from $K_d(\lambda, \text{Chl})$, and used Eq. (2). In a first step, $K_d(\lambda)$ was related to [Chl] through statistical analyses of simultaneous field data, that resulted in relationships of the generic form

$$K_d(\lambda, \text{Chl}) = K_w(\lambda) + \chi(\lambda)[\text{Chl}]^{e(\lambda)} \quad (3)$$

where $K_w(\lambda)$ represents the hypothetical K_d coefficient for pure seawater. Its lower limit is expressed as the sum of the absorption coefficient $a_w(\lambda)$ (values in Smith & Baker, 1981), and

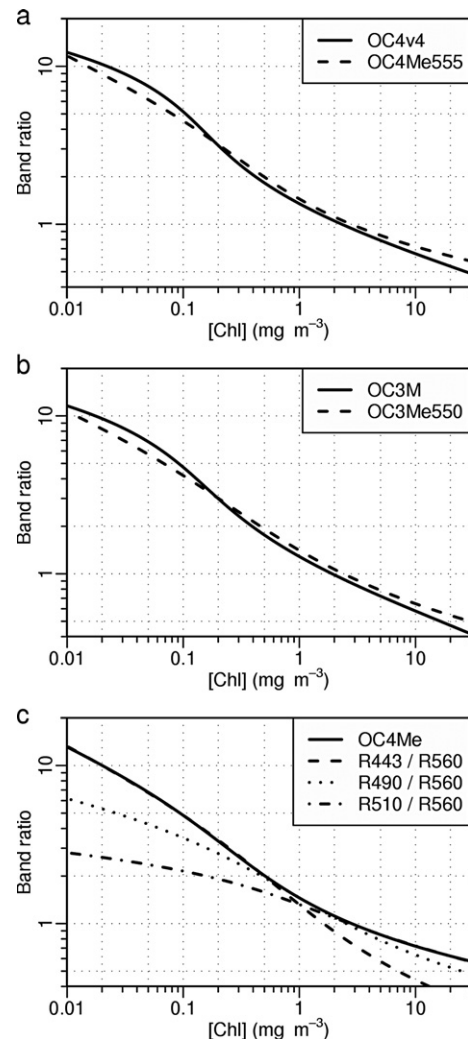


Fig. 1. Graphical representation of the chlorophyll algorithms using maximum band ratios as specified in Table 1, a) SeaWiFS chlorophyll algorithm, OC4v4, and its MERIS counterpart, OC4Me-555; b) MODIS-Aqua chlorophyll algorithm, OC3M, and its MERIS counterpart, OC3Me-550; c) Semi-analytical MERIS chlorophyll algorithm (OC4Me); this panel also displays the variations of the modeled ratios (R_{560}^{443} , R_{560}^{490} , R_{560}^{510}), which are used to construct the maximum band-ratio algorithm (to be used for the next re-processing, see MERIS-ATBD2.9, 2007).

& Gentili, 1996). Other radiometric quantities commonly in use, such as the remote sensing reflectance R_{rs} , or the normalized water-leaving radiance, nL_w , are related to the fundamental quantity R through various bidirectional factors as described in Morel and Mueller (2002) and summarized in Appendix B.

the backscattering coefficient, i.e., half of the scattering coefficient for optically pure seawater, $b_{sw}(\lambda)$ (values of Morel, 1974)

$$K_w(\lambda) = a_w(\lambda) + 1/2 b_{sw}(\lambda). \quad (4)$$

In the latest version of this approach (Morel & Maritorena, 2001, hereafter denoted by MM01), the Pope and Fry (1997) absorption values for pure water were adopted, whereas the $1/2 b_{sw}(\lambda)$ values were kept unchanged. The spectrally dependent coefficients and exponents, $\chi(\lambda)$ and $e(\lambda)$, respectively, as well as $K_w(\lambda)$, were tabulated (5 nm increment between 350 and 700 nm) in Morel and Maritorena (2001). The $\chi(\lambda)$ and $e(\lambda)$ values have been slightly revised after the incorporation of new field data (legend of Fig. 4a); they are available on the internet by ftp (ocean.e-obs-vlfr.fr, cd pub/morel, file e_chi_Kw_2006).

In both semi-analytical approaches above, the particle backscattering coefficient was modeled as follows. Field values of the particle scattering coefficient, b_p at 560 nm, were regressed against [Chl] (Gordon & Morel, 1983). This statistical relationship was revised by Loisel and Morel (1998) by considering an enlarged dataset. The resulting empirical law was thereafter combined with some assumptions regarding the backscattering probability to transform b_p into b_{bp} , the backscattering coefficient. The $R(\lambda)$ values, as well as any $R(\lambda_i)/R(\lambda_j)$ ratio (denoted by R_j^i , see Table 1), are thus related to [Chl] (for Case-1 waters only). The polynomial fits inverting these R_j^i -to-[Chl] relationships provide the semi-analytical algorithm OC4Me developed for MERIS (MERIS-ATBD 2.9, 2007). It also involves four channels and thus three ratios of spectral reflectance (graphically presented in Fig. 1c). These ratios are successively used to construct the maximum band-ratio OC4Me algorithm. It has the same polynomial structure as in Eq. (1) (coefficients in Table 2).

2.3. Compatibility of these various approaches to retrieve [Chl]

Because the wavebands differ between the three instruments (MODIS, SeaWiFS, and MERIS), the associated algorithms necessarily differ, and their comparison is not straightforward. This difficulty can be circumvented by using the aforementioned (MM01) Case-1 model. Indeed, one advantage of this hyperspectral and semi-analytical approach lies in the possibil-

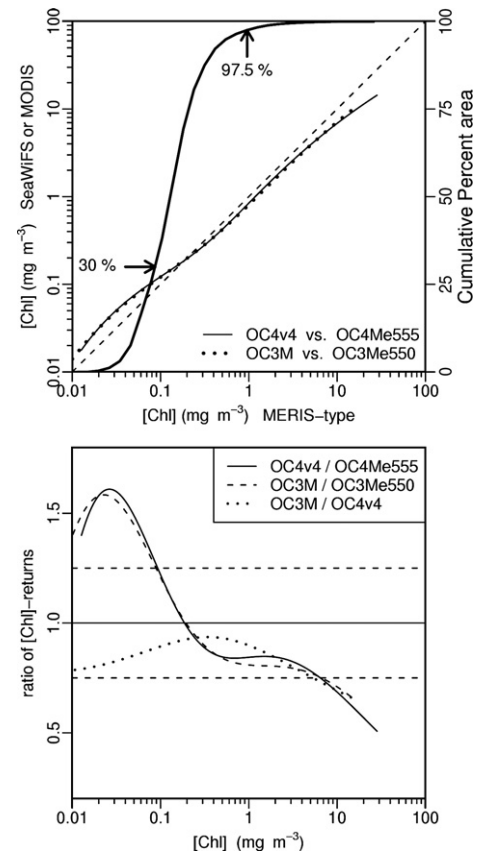


Fig. 2. Inter-comparison of the [Chl] returns. a) Returns (ordinates) of OC4v4 (SeaWiFS) and OC3M (MODIS-A), compared to the [Chl] values (abscissae), as returned by their companion MERIS-algorithms (OC4Me-555 and OC3Me-550). Note that the returns from OC4Me, OC4Me-555 and OC3Me-550, strictly follow the 1-to-1 line, because these algorithms are derived from the same bio-optical model, and thus are totally redundant. Also shown (heavy line, linear right ordinate scale as %), the cumulative frequency of occurrence within the world ocean of pixels with increasing [Chl] values (mean annual values; data from SeaWiFS; reproduced from Fig. 8 in Antoine et al., 2005). b) Ratio of the paired algorithms outputs as a function of [Chl] which is returned by the algorithm appearing in the denominators (see inset); the horizontal lines show ratios equal to 1.25, 1, and 0.75. The polynomial expressions for these curves are available on request.

Table 2
Values of the coefficients used for the algorithms in Table 1

Identifier	a_0	a_1	a_2	a_3	a_4
OC4Me ^a	0.4502748	-3.259491	3.522731	-3.359422	0.949586
OC4Me555	0.4461529	-3.291807	3.777216	-4.172339	1.415588
OC3Me550	0.3794759	-2.813392	2.021694	-2.028578	0.5173543
OC2Me555	0.4061045	-2.661052	1.300192	-3.366812	0.8125174
OK2-555	-0.826007	-1.663880	0.8132326	-2.099275	0.4937794
OK2-550	-0.8379857	-1.745822	0.901009	-2.477214	0.6758921
OK2-560 ^a	-0.8278866	-1.642189	0.90261	-1.626853	0.0885039

^a Use irradiance reflectance ratios; all others use remote sensing reflectance ratios.

ity of adjusting the algorithms to comply with the channels available on a given sensor. The green (reference) wavelength of MERIS (560 nm) can thus be replaced by 555 or 550 nm, to account for the position of the SeaWiFS and MODIS-A channels, respectively. Between these algorithms, another difference originates from the fact that the blue-to-green ratios used for the SeaWiFS and MODIS algorithms are ratios of two remote sensing reflectance, $R_{rs}^i = R_{rs}(\lambda_i)/R_{rs}(\lambda_j)$, while MERIS uses irradiance reflectance ratios, R_j^i (and the reflectances $R(\lambda_i)$ and $R(\lambda_j)$ are those when the sun-zenith angle is zero). Eq. (B-4) in Appendix B allows the transformation to be made, and actually results in small, albeit non-negligible, changes (4% at the most).

One, two, or three band-ratio techniques can be simulated, by changing the wavelengths and accounting for the switch from R_j^i to R_{rs}^i . Note that these MERIS modified algorithms, denoted by OC4Me555 and OC3Me550 (Fig. 1a and b, Table 2) are

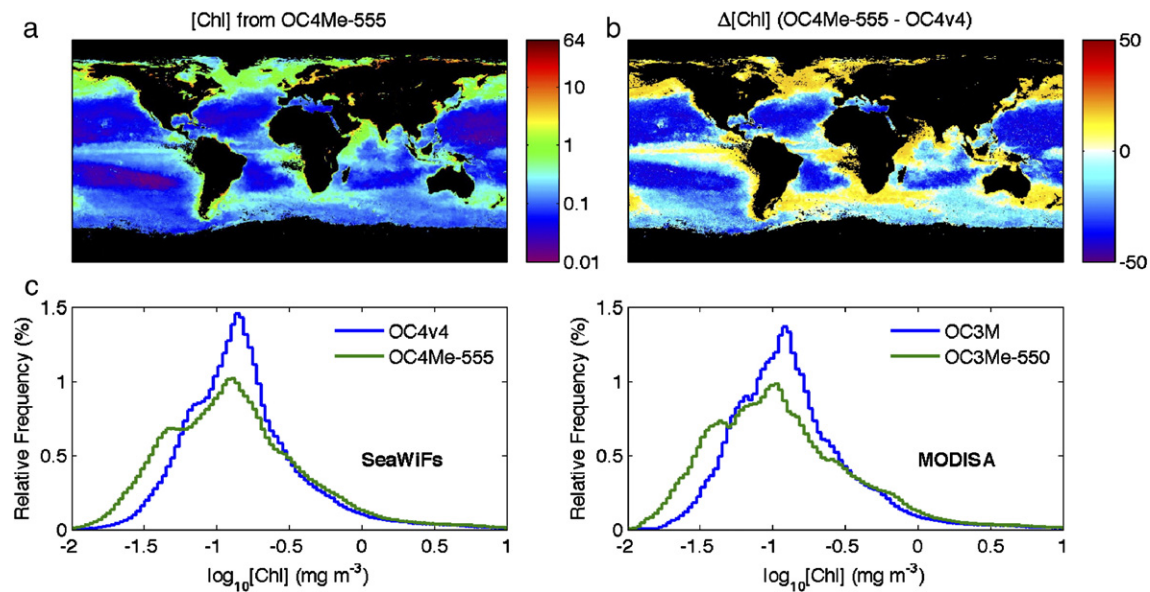


Fig. 3. SeaWiFS Level-3 composite for September 2005, a) Geographical distribution of [Chl], as produced by OC4Me-555. Because of the logarithmic scale of the color palette, the map (not shown) produced by OC4v4 is hardly distinguishable from the previous one; the differences are made apparent in the next panel. b) The unbiased relative percent difference, $\Delta[\text{Chl}] = 200 (X_2 - X_1) / (X_2 + X_1)$, where X_1 and X_2 are the [Chl] returns of OC4v4 and OC4Me-555, respectively, are mapped according to the linear color encoding, between -50 and $+50\%$, as indicated. c) The corresponding frequency distributions of X_1 and X_2 are illustrated by the histogram labelled SeaWiFS. A similar histogram for the L-3 MODIS composite (also September 2005), shows the frequency distributions when OC3M and OC3Me-550 are applied.

internally consistent, because they originate from the same hyperspectral model.

The comparison between the various algorithms is achieved by introducing the same jR_{rs} ratios into two pairs of algorithms, namely into the OC4v4–OC4Me555 pair, and the OC3M–OC3Me550 pair. The [Chl] values returned by OC4v4 and OC3M are then plotted as a function of those [Chl] values which were returned by their companion MERIS algorithm. Fig. 2a presents the result of these comparisons, and Fig. 2b the ratios of the [Chl] returns; they bring forth several useful pieces of information.

First, a satisfactory agreement (better than 20% in most of the range) exists between OC4v4 and OC3M, with a slight systematic bias, however (OC4v4 returns > OC3M returns) second, these algorithms and their MERIS counterparts agree ($\pm 25\%$) over the central part of the [Chl] range, approximately between 0.09 and 5 mg m^{-3} , and a 1:1 ratio is observed around $[\text{Chl}] = 0.22 \text{ mg m}^{-3}$, that is close to the median value for the whole ocean (Fig. 2a), and to the mean [Chl] value for deep oceanic waters, (0.193 mg m^{-3} , Wang et al., 2005). Inside this central range, the divergences (positive or negative) remain at least within the variance ($\pm 35\%$) observed when the field data points are plotted along with the curves representing the algorithms (Figs. 8e and 9e in O'Reilly et al., 2000; Fig. 11a and b in Morel & Maritorena, 2001), as well as within the realistic goal of ocean color sensors. Third, significant discrepancies appear in oligotrophic waters (when $[\text{Chl}] < 0.09 \text{ mg m}^{-3}$), where the [Chl] returns from SeaWiFS and MODIS-A are systematically higher than the MERIS-type returns; the excess may reach 50% at the lower limit of the [Chl] range ($\sim 0.02 \text{ mg m}^{-3}$). As demonstrated by the cumu-

lative frequency curve (also shown in Fig. 2a), waters with $[\text{Chl}] < 0.1 \text{ mg m}^{-3}$ would represent about 30% of the whole ocean, in terms of area, but less than 10% in terms of chlorophyll biomass. Such a systematic divergence, however, must be accounted for, in particular if a merging of the data is envisaged.

Fourth, in eutrophic waters, the situation is inverted, and the MERIS-type returns exceed both those of MODIS-A and SeaWiFS. In this domain of concentration, which represents less than 1% of the oceanic area (when $[\text{Chl}] > 5 \text{ mg m}^{-3}$), the natural variability in the optical properties within such high [Chl] waters generally degrades the competence of any algorithm; furthermore, the variations of the spectral reflectance ratios per unit of [Chl] become minute in this range, and thus reduce the sensitivity of all algorithms.

An example providing the geographical distributions of the divergences between the algorithms outputs is displayed in Fig. 3 (the same R_{rs} are introduced in the paired algorithms). It confirms what can be expected from Fig. 2b. The color plate shows the location and magnitude of opposite differences (displayed as unbiased relative percent differences). Negative differences occur in the wide oligotrophic subtropical gyres, whereas positive differences occur in the high latitude belts, as well as along the equatorial divergence. The frequency distributions of the [Chl] values from SeaWiFS and MODIS-A, as obtained through their nominal algorithms, or through their MERIS type counterparts, are also displayed as histograms. As expected, the number of pixels with low [Chl] values are more represented when the MERIS type algorithms are operated, with also the result that the peak centered on $\sim 0.15 \text{ mg m}^{-3}$ is somewhat erased and slightly shifted.

In summary, under the proviso that the atmospheric corrections are perfectly effected for all sensors and that the radiometric calibrations are accurate, the retrieved [Chl] values agree over an extended range, at least within the generally expected accuracy for this concentration (O'Reilly et al., 2000). It is worth recalling that both types of algorithms (either empirical or semi-analytical) fail in Case-2 coastal waters, where optically influential materials (suspended mineral particles, yellow substance drained from land), that are not correlated with the algal concentration, interfere with the retrieval of [Chl], and most often lead to [Chl] overestimates.

3. K_d algorithms

Two approaches were also developed to assess the diffuse attenuation coefficient, as briefly presented below.

3.1. First method

An empirical approach, parallel to that developed for [Chl], was proposed by Austin and Petzold (1981, 1986). It consisted of relating directly $K_d(\lambda)$ to a ratio, ρ_{ij} , of observed upward radiances (L_w) at two wavelengths, i and j . The statistical

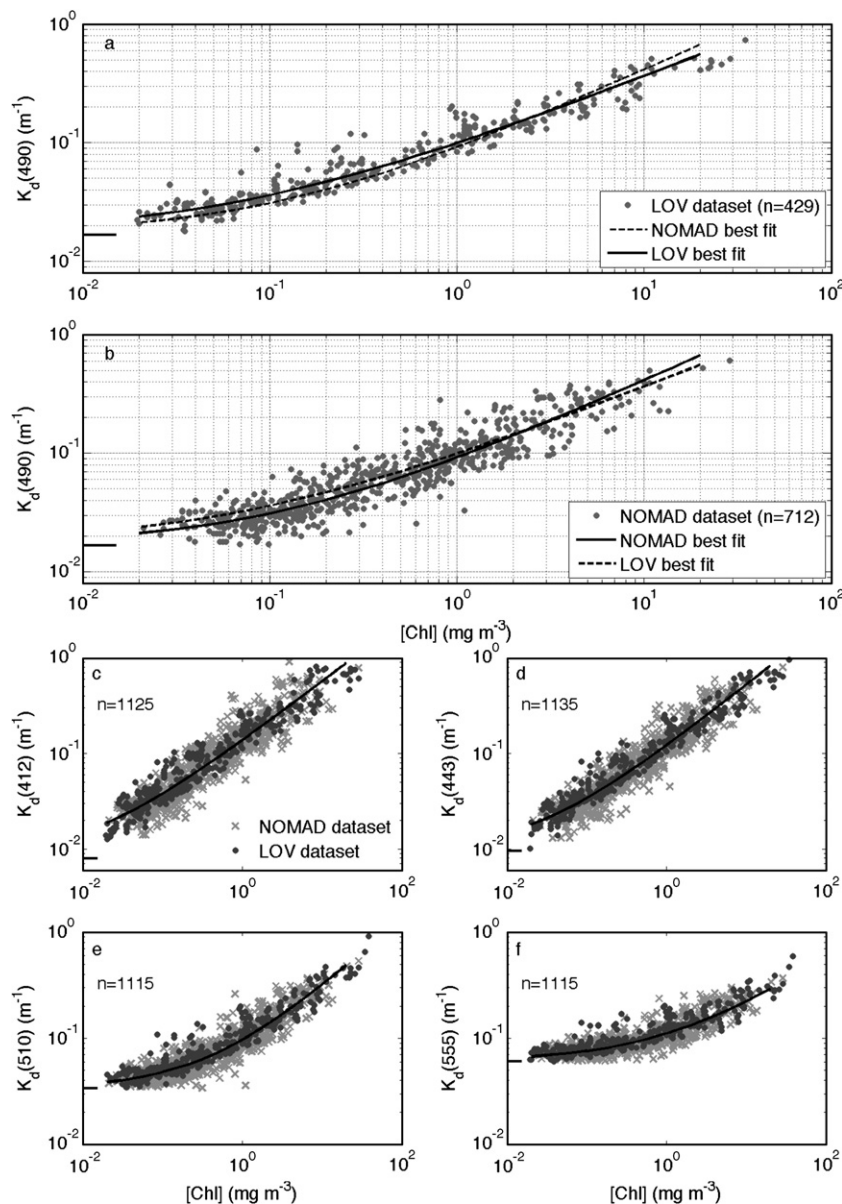


Fig. 4. The $K_d(490)$ coefficient as a function of [Chl] in Case-1 waters. a) The data shown are those already used in Morel and Maritorena ($N=298$), to which are added 156 new data pairs determined during more recent cruises (see Appendix C). This dataset is denoted by "LOV dataset". The solid curve which represents the best fit corresponds to $K_d(490)=0.0166+0.08253 [\text{Chl}]^{0.6529}$, with $N=454$, $R^2=0.983$, $\text{RMSE}=0.09195$, on the log-transform data. b) NOMAD $K_d(490)$ data as a function of [Chl]. The NOMAD data are sorted to keep only those with HPLC determinations of [Chl]. The solid curve represents the best fit and corresponds to $K_d(490)=0.0166+0.07197 [\text{Chl}]^{0.7555}$, with $N=712$, $R^2=0.917$, $\text{RMSE}=0.1285$, on the log-transform data. The value corresponding to pure water is indicated by a tick in each panel. c to f) Merged data NOMAD+LOV, for other specified wavelengths; in each panel, the curves represent the best fits for the merged data; the corresponding equations and statistics are given in Table 4.

analysis of the existing field data resulted in relationships (then used as algorithms for CZCS) of the generic form

$$K_d(\lambda) = K_w(\lambda) + A(\rho_{ij})^B. \quad (5)$$

In the original work, i and j were 443 and 550 nm, respectively (in correspondence with the CZCS channels) and λ was either 490 or 520 nm. The constant term $K_w(\lambda)$, is (as above in Eq. (4)) the coefficient for pure seawater, and was given the values 0.022 and 0.044 m^{-1} , at 490 and 520 nm, respectively. Based on a more extended dataset, this relationship was later revisited (Mueller, 2000), and transformed into

$$K_d(490) = 0.016 + 0.1565 (r_{490,555})^{-1.540} \quad (6)$$

where $r_{490,555}$ is now the ratio of *normalized water-leaving radiances* (nL_w) at 490 and 555 nm, and the term 0.016 m^{-1} is a revised value of K_w at 490 nm. This constant term is suppressed in the most recent algorithm in use for SeaWiFS (Werdell, 2005), and the best fit is simply expressed as

$$K_d(490) = 0.1853 (r_{490,555})^{-1.349}. \quad (7)$$

3.2. Second method

Regression analyses were performed (Morel, 1988) for Case-1 waters, for all wavelengths between 400 and 700 nm, on the log-transforms of [Chl] and of the quantity K_{bio} , defined as the difference $[K_d(\lambda) - K_w(\lambda)]$. With an increased number of field data ($N=298$), the MM01 statistical study led to the following relationship (of the form of Eq. (3))

$$K_d(490) = 0.0166 + 0.07242[\text{Chl}]^{0.68955}$$

where the adopted constant for pure water (0.0166 m^{-1}) slightly differs from that in Eq. (6). With the addition of recent observations (LOV dataset, Appendix C, and Fig. 4a), the above empirical relationship is again slightly modified (new parameters in the legend).

The completely independent NOMAD dataset (Werdell & Bailey, 2005; Appendix C) is similarly displayed in Fig. 4b. The best fit for each of these datasets are practically undistinguishable, with similar parameters and root mean square errors (RMSE) (given in the legend), so that it is logical to merge the two datasets. Submitted to regression analysis, this merged dataset ($N=1166$, $R^2=0.9298$ and $\text{RMSE}=0.1178$) leads to the following expression which is thereafter adopted, namely

$$K_d(490) = 0.0166 + 0.0773 [\text{Chl}]^{0.6715}. \quad (8)$$

It is important to note that $K_d(490)$ can barely exceed 0.5 m^{-1} in Case-1 waters, as this value is reached when $[\text{Chl}] \sim 20 \text{ mg m}^{-3}$. Higher values are often observed in coastal waters, which are beyond the applicability of the above relationships. A new method has been recently developed (Lee et al., 2005) to remove this limitation and to cope with such coastal, and more complex situations.

3.3. Compatibility of these approaches for the retrieval of K_d

The $K_d(490)$ coefficient can thus be computed i) either by using the $r_{490,555}$ ratio and Eq. (6), or preferably, the recent Eq. (7), or ii) by operating Eq. (8) with [Chl] retrieved separately. These two approaches, however, cannot provide identical $K_d(490)$ values for theoretical reasons examined below.

The polynomial expressions that relate blue-to-green ratios to [Chl] (both empirical and semi-analytical, such as OC4v4 and OC4Me, respectively) account for the sigmoid-shaped curve displayed in log–log space (see Fig. 1). This behavior was explained by Gordon and Morel (1983, see their Fig. 8) by the fact that asymptotic values (provided in Table 3) must exist when [Chl] tends toward 0 (pure water), or toward very high values (hypothetical “pure phytoplankton” medium). By a similar rationale, this sigmoidal character must be maintained (in log–log space) when relating K_{bio} to any reflectance ratio.

This is indeed the case as demonstrated by Fig. 5. The curve (denoted by “present study”) is obtained by generating a series of [Chl] values from a series of discrete R_{555}^{490} values through the use of OC2Me-555. Then, these [Chl] values are introduced into Eq. (8) to produce the quantity $K_{bio}(490)$. The solid curve in Fig. 5 which shows the variation of $K_{bio}(490)$ as a function of R_{555}^{490} includes, as expected, an inflexion point. Such a sigmoidal shape is inconsistent with the form of the empirical Eq. (6), which linearly relates $\log(K_{bio})$ to $\log(r_{490,555})$; it also deviates from the Werdell (2005) relationship both in the domains of very low and of high K_d values. Ostensibly, this sigmoidal

Table 3
Tentative asymptotic values of the reflectance ratios, R_j^i

i	j		
	560	555	550
R_j^i for $[\text{Chl}] \rightarrow 0$			
443	17.91	15.95	15.87
490	6.79	6.05	6.02
510	2.73	2.43	
R_j^i for $[\text{Chl}] \rightarrow \infty$			
443	0.317 (0.329)	0.350 (0.340)	0.372 (0.355)
490	0.484 (0.481)	0.539 (0.495)	0.573 (0.527)
510	0.589 (0.591)	0.650 (0.609)	0.692 (0.636)

When $[\text{Chl}] \rightarrow 0$, they are computed as

$$\{b_{bw}(i)/[b_{bw}(i) + a_w(i)]\} / \{b_{bw}(j)/[b_{bw}(j) + a_w(j)]\},$$

where $a_w(i \text{ or } j)$ and $b_{bw}(i \text{ or } j)$ are the absorption and backscattering values for pure seawater at the wavelengths $\lambda=i$ or j , taken from Pope and Fry (1997), and Morel (1974), respectively. Such computation assume that the f'' factors (in Eq. (2')) are the same for the two wavelengths i and j (which is questionable).

When $[\text{Chl}] \rightarrow \infty$, the limiting values are tentatively computed as the ratio $a_p(j)/a_p(i)$, i.e. the ratio of the particle absorption when $[\text{Chl}]=10 \text{ mg m}^{-3}$, as adopted from Bricaud et al. (1998). This way of computing assumes that the absorption by water (and yellow substance) has become negligible compared to that of the phytoplanktonic assemblage, and that backscattering is neutral (which is probably not true). The other way consists (values in parenthesis in the table) of using the K_{bio} values, also for $[\text{Chl}]=10 \text{ mg chl m}^{-3}$, as tabulated in Morel and Maritorena (2001).

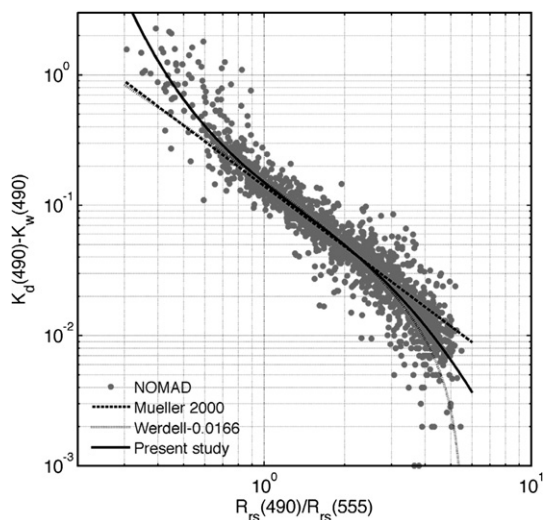


Fig. 5. The relationship between $K_{\text{bio}}(490)$ ($=K_d(490) - K_w(490)$), and the ratio ${}^{490}_{555}R_{\text{rs}}$. This curve (solid line) which corresponds to the algorithm OK2-555 (Tables 1 and 2), is drawn on the top of the NOMAD data. Also shown are the Mueller (2000) algorithm (Eq. (6)), and the Werdell (2005) algorithm (Eq. (7)), to which the constant K_w value is subtracted for comparison. Note that the two lines (Mueller and Werdell) corresponding to Eqs. (6) and (7) are superimposed in the domain of moderate and high K_d values.

shape accounts much better for the distribution of the field data (also displayed in Fig. 5) over their entire range.

Given the superiority of this shape, the proposition put forward here is to abandon the linear fits (expressed by Eqs. (6) or (7)), and to use the new curvilinear relationship instead. The polynomial fit to this curve provides the OK2-555 algorithm. Accounting for the various possible green wavelengths, the OK2 (-560 , -555 , -550) algorithms are also provided in Table 2. The differences induced by the replacement of Eq. (7) by an OK2-type algorithm will be examined below, by considering field data or ocean color imagery.

It must be noted that using an algorithm of the OK2 type in lieu of Eqs. (6) or (7) means that the direct empirical approach is de facto abandoned, and instead is replaced by a method where [Chl] is an implicit intermediary. Indeed, the development of OK2 has actually involved the $[\text{Chl}] \leftrightarrow K_d(490)$ empirical relationship.

3.4. Practical solutions

Two differing methods to derive K_d can practically be envisaged. The first one uses as input the ${}^{490}_{555}R_{\text{rs}}$ ratio, with, as said above, two possible branches, either the empirical Eq. (7) or preferably the semi-analytical OK2 algorithm. The second method uses an independent assessment of [Chl] and then Eq. (8). Several inter-comparisons are possible, and selected combinations of available algorithms are commented below in reference to panels in Fig. 6.

a) An evaluation of the first method is provided by Fig. 6a, which basically serves as an illustration of the performance of the curvilinear (OK2-555) algorithm when applied to an

independent dataset. The reflectance ratios (${}^{490}_{555}R_{\text{rs}}$) taken from NOMAD are used as inputs into the OK2-555 algorithm, then the resulting $K_d(490)$ values are compared to the actual field values, also taken from NOMAD. The agreement between the retrieved and actual values is excellent, without significant bias. Interestingly, the scatter of the points starts to increase notably for $K_d(490) > 0.4 \text{ m}^{-1}$ ($[\text{Chl}] > 10 \text{ mg m}^{-3}$), likely outside of the Case-1 water domain.

- b) The second method can be tested (Fig. 6b), again by using the NOMAD data. The (three) appropriate ${}^jR_{\text{rs}}$ values are extracted from the NOMAD database and [Chl] is computed via OC4Me-555. These values are then introduced into Eq. (8) to derive $K_d(490)$. The resulting values can be compared to those derived from OK2-555 applied to the single ${}^{490}_{555}R_{\text{rs}}$ ratio. Because the two algorithms (OC4Me-555 and OK2-555) are basically derived from the same bio-optical model, an overall agreement exists between the two sets of $K_d(490)$ values. The scatter, which however occurs at the two ends of the K_d range, probably reflects some inconsistencies among the three experimental ${}^jR_{\text{rs}}$ values; indeed, it is considerably reduced when the same ${}^{490}_{555}R_{\text{rs}}$ ratio is used for the two methods, i.e., in the middle [Chl] range ($0.4\text{--}2.5 \text{ mg m}^{-3}$, approximately), when K_d is between 0.06 and 0.16 m^{-1} .
- c) The same comparison can be made (Fig. 6c) by using Eq. (7), instead of OK2-555, to retrieve $K_d(490)$. In this case, systematic departures appear at both ends of the range which actually mimic the divergences already highlighted by Fig. 5 (the values provided by Eq. (7) are lower than those provided by OK2-555, except in the middle range where they coincide).
- d) In Fig. 6d the K_d returns both via [Chl], yet when using either OC4v4 and OC4Me-555 are compared. Not surprisingly, the divergences previously observed (Fig. 2b) regarding the retrieved [Chl], logically translate into similar discrepancies between the calculated $K_d(490)$ values. As a consequence, the shape of the curve in Fig. 6d bears a resemblance with the one in Fig. 2a. Because K_d barely exceeds the value of pure water at low [Chl], the non-negligible differences in the [Chl] estimates within this range cannot generate a notable difference in K_d . In contrast, at high [Chl], the [Chl] estimates via OC4v4 (lower than those derived from OC4Me-555, by $\sim 20\%$ — see Fig. 2b) generate markedly lower K_d values. In the middle of the [Chl] range (when $[\text{Chl}] < 3 \text{ mg m}^{-3}$ and $K_d < 0.2 \text{ m}^{-1}$), the differences in K_d practically vanish.

Examples of practical application of the above algorithms and methods to ocean color imagery are provided in Fig. 7. In Fig. 7a, the $K_d(490)$ values are produced via Eq. (7) applied to the R_{rs} data from MODIS-A (monthly average for September, 2005). The OK2-550 algorithm is applied to the same R_{rs} data, and the relative differences in $K_d(490)$ are visualized in Fig. 7b. The explanation for the differences is to be found in Fig. 5; when $K_{\text{bio}}(490)$ is below 0.035 m^{-1} (i.e., when $K_d(490) < 0.05 \text{ m}^{-1}$), the output of Eq. (7) is below that of OK2. Therefore, in the extended subtropical oligotrophic gyres, the

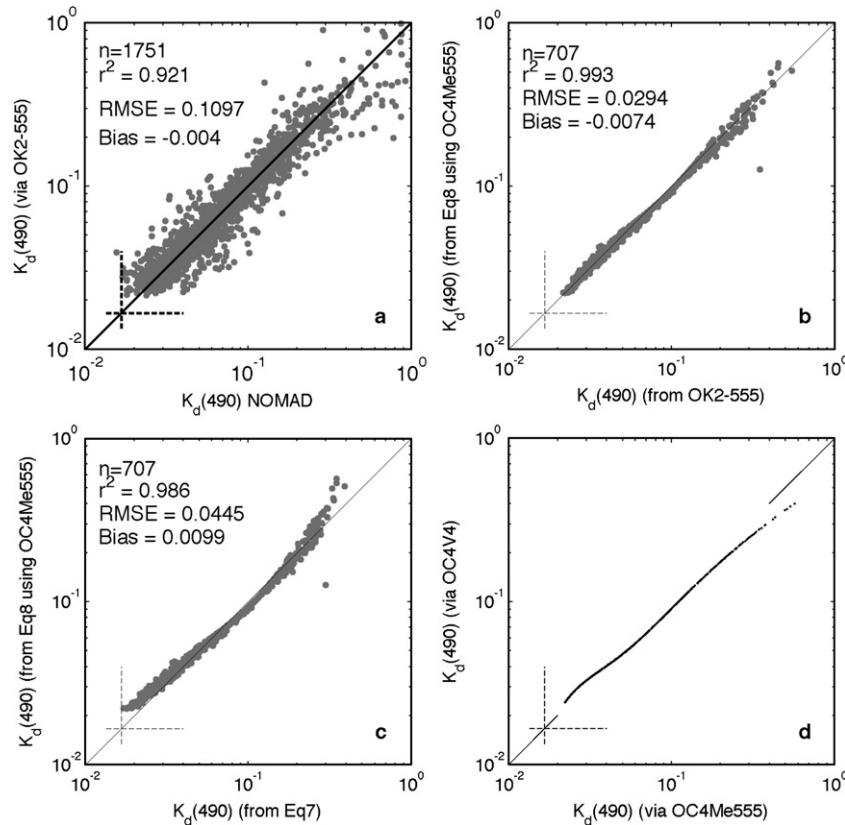


Fig. 6. a) Application of Method 1 to the NOMAD data, which makes use of $^{490}_{555}R_{rs}$ with the OK2-555 algorithm. The lower limit for $K_d(490)$ ($=0.0166 \text{ m}^{-1}$) is also indicated (dashed lines) in this panel and the following ones. b) Comparison of the $K_d(490)$ estimates via Method 2 (ordinates, algorithm OC4Me555, with [Chl] as intermediate link), and Method 1 (abscissae, OK2-555 algorithm, making a direct use of the ratio $^{490}_{555}R_{rs}$). c) Ordinates as in panel c, but the $K_d(490)$ values in abscissae are obtained through the empirical Eq. (7). d) Application of Method 2 on NOMAD data, and a comparison of the $K_d(490)$ values when [Chl], the intermediate link, is either produced by OC4v4 (ordinate axis) or by OC4Me555 (abscissae axis).

difference (OK2–Eq. (7)) is positive. The same situation happens in some restricted areas where $K_d(490)$ is high enough ($>0.15 \text{ m}^{-1}$, e.g., in coastal zones of the Northern hemisphere). Elsewhere, the differences are close to zero or slightly negative. The extension toward smaller $K_d(490)$ values when using Eq. (7) is clearly confirmed by all the histograms (see below).

Another kind of comparison (Fig. 7c); shows the relative percent difference between the $K_d(490)$ values obtained by using [Chl] (via OC3Me-550) as input into Eq. (8), and those directly obtained through Eq. (7). The geographical distribution of the relative differences (Eq. (8)–Eq. (7)) is similar to that in panel 7b, although the differences are slightly more accentuated. These enhanced differences are predictable from the comparison between Fig. 6c and b; indeed, the departure from the 1:1 line, at both ends of the $K_d(490)$ range, is more accentuated in Fig. 6c than in b.

The $K_d(490)$ values, when derived via all algorithm combinations for MODIS-A and SeaWiFS, are comparatively displayed as histograms of frequency of occurrences (Fig. 7e). In all cases and as anticipated, the histograms corresponding to the application of Eq. (7) expand toward the domain of lower values more than do the other algorithms. Generally, when Eq. (7) and OK2 algorithms are employed, the distributions peak around the same K_d value (but note the differences between SeaWiFS and MODIS-A histograms). Finally, the application of

Eq. (8) shifts the peak toward larger K_d values, when the nominal algorithms (OC4v4 and OC3M) are operated to retrieve [Chl]. When the MERIS-type algorithms (OC3Me-550 and OC4Me-555) are used, this relative shift disappears. Also, in this case, the three distributions (via Eqs. (7) and (8) and OK2) practically coincide and are similarly centered (on ~ 0.026 and 0.030 m^{-1} for MODIS-A and SeaWiFS, respectively). This coincidence is not surprising since the semi-analytical algorithms (OC4Me-555 and OC3Me-550) are fully compatible with Eq. (8) (actually with the Equation for the LOV data given in the legend of Fig. 4a, which anyway is very close to Eq. (8)). In contrast, the non-coincidence when the nominal OC4v4 and OC3M algorithms are used, obviously originates from the differing [Chl] returns, previously discussed (cf. Fig. 2).

With respect to the K_d coefficient, an additional point merits consideration. There exist in the literature some misinterpretations of this parameter when it is derived from remote sensing observation. In effect, it is sometimes believed that K_d is an independent variable, because it results from the use of a specifically developed algorithm (like Eq. (7)). This algorithm, however, and the [Chl] algorithm, are based on a ratio of reflectances, so that by eliminating this ratio between the two algorithms, a univocal relationship between K_d and [Chl] necessarily emerges. This redundancy (or mathematical correlation) between the two quantities, which was previously noted by Gordon and

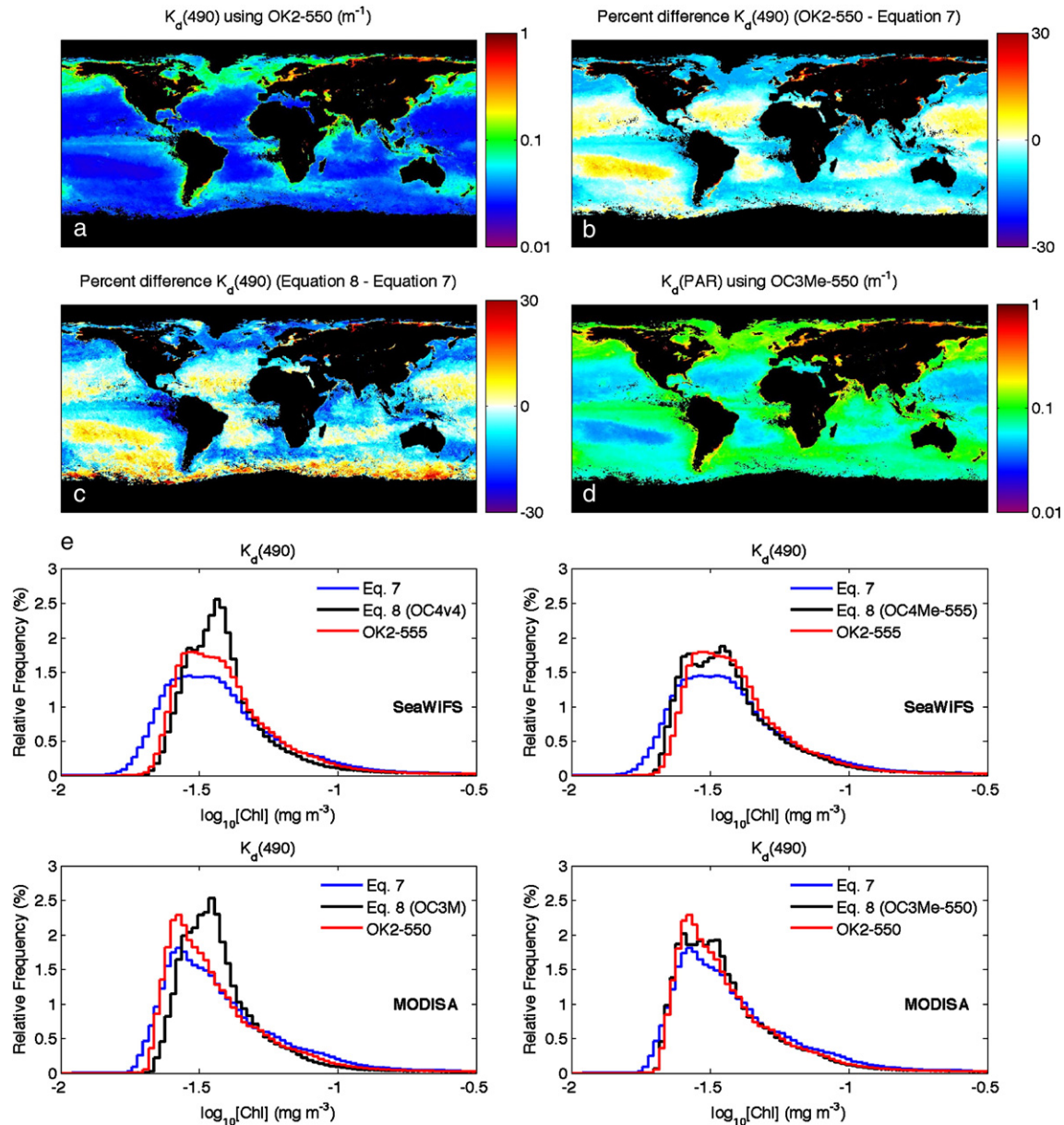


Fig. 7. Comparison of various $K_d(490)$ estimates using a monthly MODIS L-3 composite for September 2005. a) Returns from Eq. (7), b) Unbiased relative percent differences between the returns of the OK2-550 algorithm and the $K_d(490)$ values via Eq. (7), already displayed in a. c) Unbiased relative percent differences between the returns of Eq. (8) applied to $[\text{Chl}]$ values obtained through the OC3Me-550 algorithm, and the $K_d(490)$ values displayed in a. d) $K_d(\text{PAR})_2$ obtained via Eq. (9') for the MODIS composite (September 2005) and when $[\text{Chl}]$ is obtained through OC3M, e) Frequency distribution histograms for various possible combinations; SeaWiFS data are successively processed using Eq. (7), via OK2, and also by using $[\text{Chl}]$ as intermediary (Eq. (8)), when $[\text{Chl}]$ is derived either by OC4v4 or by OC4Me-555; likewise, MODIS data are processed using Eq. (7), and OK2, and also by using $[\text{Chl}]$ as intermediary (Eq. (8)), as derived either by OC3M or by OC3Me-550.

Morel (1983, page 64), is often ignored in discussions or applications, where the retrieved K_d and $[\text{Chl}]$ are erroneously considered as independent variables or truly distinct information.

3.5. From $K_d(490)$ to $K_d(\text{PAR})$

Through its inverse, $K_d(490)$ provides the depth from which 90% of the emerging signal at 490 nm originates (Gordon & McCluney, 1975); it thus allows the thickness of the layer “seen” by the sensor at this wavelength to be estimated

remotely. This is one of the main rationales for its derivation. In some primary production modeling approaches, and despite the weakness of such an approximation, $K_d(490)$ was also proposed (Campbell, 2004) as a surrogate for the downward diffuse attenuation coefficient for the Photosynthetically Available Radiation, denoted by $K_d(\text{PAR})$; recall that PAR is the polychromatic radiation within the entire 400–700 nm spectral range (Tyler, 1966).

A series of empirical $K_d(\lambda)$ – $[\text{Chl}]$ relationships (as in Eq. (8)) have been established using the LOV dataset for all

wavelengths between 400 and 700 nm (available on the internet). Within the frame of this K_d hyperspectral model, the propagation of PAR and thus the $K_d(\text{PAR})$ values can be predicted. Therefore, it seems logical to rely on the $K_d(490)$ value to infer $K_d(\text{PAR})$, rather than using $K_d(490)$ as an ill-defined proxy.

This extension toward $K_d(\text{PAR})$ is not straightforward, if envisaged under all its aspects. Indeed, the relationship between the near surface $K_d(490)$ and $K_d(\text{PAR})$ values depends on the spectral composition of the radiation incident upon the sea surface. In addition, $K_d(\lambda)$ depends on the sun-zenith angle, θ_s , in clear skies, (see Fig. 3 in Morel & Gentili, 2004). The theoretical variations of $K_d(490)$ and $K_d(\text{PAR})$ with solar angle and over the whole [Chl] range are illustrated by Fig. 8a. In this figure, $K_d(\text{PAR})$ is computed for a layer of thickness equal to $[K_d(490)]^{-1}$. As expected, in blue waters with low [Chl], the polychromatic $K_d(\text{PAR})$ is about twice $K_d(490)$, and the difference lessens for waters becoming greener with increasing [Chl]. Both $K_d(490)$ and $K_d(\text{PAR})$ increase with increasing θ_s ; their ratio, however, remains essentially constant (within $\pm 2\%$), whatever θ_s . Their inter-relationship is therefore very robust, and rather insensitive to the sun position. The best fit for $K_d(\text{PAR})_1$ (subscript 1 when the thickness of the layer considered is equal to $[K_d(490)]^{-1}$) leads to

$$K_d(\text{PAR})_1 = 0.0864 + 0.884 K_d(490) - 0.00137 [K_d(490)]^{-1}. \quad (9)$$

If the water body is supposed to be homogeneous, $K_d(490)$ depends only weakly on the thickness of the layer under consideration; only the progressive change in the directivity of the downward radiant flux (as expressed by μ_d , the average cosine for this flux) may cause slight changes in $K_d(490)$. On the contrary, and because of its polychromatic nature, $K_d(\text{PAR})$ depends strongly on the thickness of the layer considered. Because red radiation is quickly absorbed in the top layer, the PAR domain actually narrows down deeper in the water column, and concentrates around the least attenuated wavelength. As a result, for (almost) the same $K_d(490)$, $K_d(\text{PAR})$ significantly decreases when the thickness of the layer is increased. This is made clear by Fig. 9b; $K_d(\text{PAR})_2$ (with subscript 2) is now computed for a layer with a thickness equal to $2[K_d(490)]^{-1}$. The $K_d(\text{PAR})_2$ – $K_d(490)$ relationship becomes

$$K_d(\text{PAR})_2 = 0.0665 + 0.874 K_d(490) - 0.00121 [K_d(490)]^{-1}. \quad (9')$$

The predictive skill of this relationship is verified on an independent dataset (SCAPA; see Appendix C); these data are compared to Eq. (9') in Fig. 9c. Note that some scatter and systematic divergence (see inset) appear when $K_d(490)$ is $> 0.3 \text{ m}^{-1}$ and $[\text{Chl}] > 7 \text{ mg m}^{-3}$. (likely in coastal waters). In such cases, the $2[K_d(490)]^{-1}$ layer involved is rather thin ($< 6.66 \text{ m}$), and the accuracy of the K_d determinations over this interval becomes problematic and sensitive to the binning procedure.

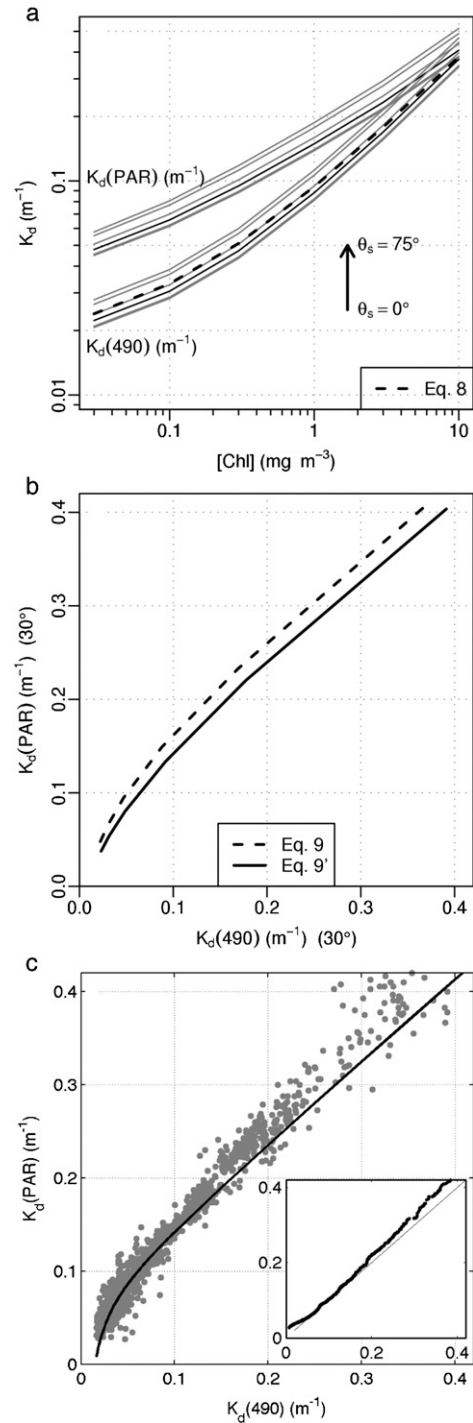


Fig. 8. a) Variations with [Chl] of $K_d(490)$ and $K_d(\text{PAR})$. The two families of curves have been generated through radiative transfer computations (Morel and Gentili, 2004) for various solar zenith angles (θ_s , from 0 to 75°) in a standard blue sky. The K_d coefficients (for 490 and for PAR) have been computed for the layer corresponding to the first penetration depth (i.e., of thickness $[K_d(490)]^{-1}$, Gordon and McCluney, 1975). The empirical $K_d(490)$ –[Chl] relationship (Eq. (8)), which is also displayed, agrees with the theoretical ones in the middle of the θ_s range (~ 30 – 45°). b) $K_d(\text{PAR})$ as a function of $K_d(490)$, both for $\theta_s = 30^\circ$, when the thickness of the layer considered is either $[K_d(490)]^{-1}$, or $2[K_d(490)]^{-1}$, in correspondence with Eqs. (9) or (9'), respectively. c) $K_d(490)$ and $K_d(\text{PAR})$ data for the $2[K_d(490)]^{-1}$ thick layer from the Self Consistent AOP Profiles Archives (S.B. Hooker, Appendix C); the curve corresponds to Eq. (9'). Inset: quantile to quantile plot of actual $K_d(\text{PAR})$ versus $K_d(\text{PAR})$ as predicted via Eq. (9').

The above relationship dramatically differs from those used in Rochford et al. (2001), apparently because of a misinterpretation of the results in the study of Zaneveld et al. (1993). Actually, this study deals with optical thicknesses (for 490 or PAR radiation) for variously increasing optical-depth intervals, not with the K_d coefficients in the upper layer.

The geographical distribution of $K_d(\text{PAR})_2$, as derived through Eq. (9'), is displayed in Fig. 7d. It also shows the notable shift of $K_d(\text{PAR})_2$ toward higher values compared with those of $K_d(490)$. The possibility of estimating $K_d(\text{PAR})_2$ for the upper layer is useful in the prediction of the heating rate by solar radiation, and thus for the modeling of the mixed layer dynamics (Woods et al., 1984). Indeed, the solar IR radiation ($\sim 57\%$ at the sea level) is totally absorbed within a very thin layer (~ 1 m). The visible radiation ($\sim 43\%$ of the total radiation) penetrates much deeper. However, 87% of this energy (corresponding to

$(1 - e^{-2}))$ is already absorbed within an upper layer, the thickness of which, denoted by $Z_{hl} = 2[K_d(\text{PAR})_2]^{-1}$. In total, about 95% of the solar heat deposition is realized within this Z_{hl} thick layer (heated layer).

At the two extremes of the [Chl] range (0.01 and 10 mg m^{-3} , for instance), the $K_d(\text{PAR})_2$ values (Eq. (9)) amount to 0.024 and 0.39 m^{-1} , respectively, and lead for the heated layer, to Z_{hl} values of about 84 and 5 m, respectively. The conversion of $K_d(490)$ into $K_d(\text{PAR})$ and then into Z_{hl} is only possible under the proviso that Case-1 bio-optical properties are involved, (the above equations do not apply in Case-2 waters) and that the [Chl] vertical structure is not irregularly structured (see below). An example of application of the above technique to MODIS-A data is provided (Fig. 12a). Although the thinner and thicker heated layers are geographically located as it can be anticipated, the amplitude of variations in Z_{hl} within the global ocean reveals to be remarkably wide.

4. Miscellaneous applications

It is tempting to go farther and extrapolate information about the upper layer toward deeper levels not “seen” by the sensor. It is merely stating the obvious to say that uncertainties will grow in such attempts and that auxiliary information will be needed. This information can only originate from previous oceanographic studies having dealt with the full vertical structure of the water column. Two “extrapolations” are examined here, i) the depth of the euphotic layer (Z_{eu}), which is a crucial information in primary production modeling (e.g., Carr et al., 2006), and ii) the depth of the disappearance of the Secchi disk (Z_{sd}), which is used as a visual index of water quality, and for which a long-term historical record does exist.

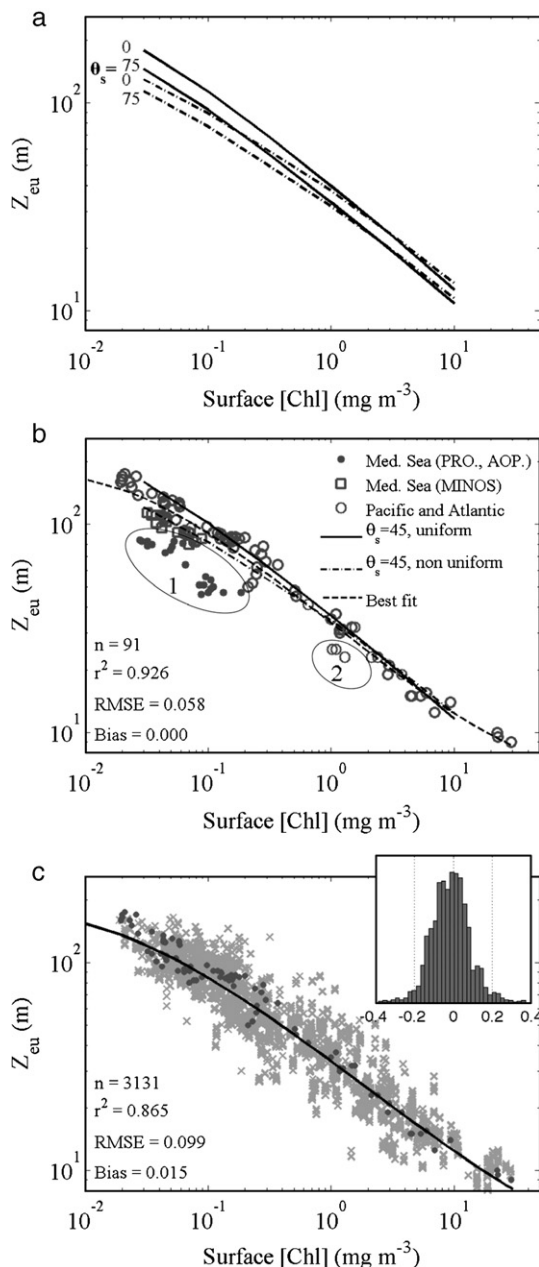


Fig. 9. a) Depth of the euphotic layer, Z_{eu} , as a function of $[\text{Chl}]_{\text{surf}}$ (redrawn from Morel and Gentili, 2004). The solid curves are for structured [Chl] vertical profiles that include a deep chlorophyll maximum, whereas the dotted curves are for uniform profiles. In each pair, the upper and lower curves are for a sun zenith angle $\theta_s = 0^\circ$ or 75° , respectively. b) Recent field determinations of Z_{eu} , and $[\text{Chl}]_{\text{surf}}$ in Case-1 waters. The total number of data pairs is 117, and includes 53 pairs from Pacific (BIOPEX cruise), 31 from Atlantic (EUMELI 3 and 4, PROSOPE and BENCAL cruises), and 33 are from the Mediterranean Sea (PROSOPE, AOPEX and MINOS cruises). These data encompass a wide range of situations from hyper-oligotrophic to eutrophic waters. Apart from the MINOS cruise data (squares), the Mediterranean data (within ellipse 1) generally depart from the average trend for various reasons (Claustre et al., 2002); regarding the Z_{eu} level, the observed departure mainly originates from the position of the DCM, which actually is less deep than the modeled one; for instance, double peaked maxima occur at 40 and 55 m in the North Western Mediterranean basin (AOPEX), while the value, modeled from $[\text{Chl}]_{\text{surf}}$, would be close to 70–80 m. The particular behavior of the data in a mesotrophic situation off Mauritania (Eumeli 4, ellipse 2) is associated with the dominance of *Synechococcus* in the phytoplanktonic assemblage (Morel, 1997). Superimposed are the two curves (uniform and structured vertical profiles) as in panel a, but for $\theta_s = 45^\circ$, and also the curve corresponding to the best fit

$$\log_{10} Z_{eu} = 1.524 - 0.460X - 0.00051X^2 + 0.0282X^3 \quad (X = \log_{10} [\text{Chl}]_{\text{surf}})$$

c) Grey symbols: $[\text{Chl}]_{\text{surf}}$ and Z_{eu} values, from the SCAPA archive; superimposed (black dots) data from the panel b (except those in the ellipses). The curve represent the best fit for merged data (Eq. (10) in the text). In inset, the frequency distribution of the \log_{10} of the ratio (measured Z_{eu})/(predicted Z_{eu} via Eq. (10)).

4.1. Depth of the euphotic layer

By convention, the bottom of the euphotic layer, Z_{eu} , is defined as the depth where E_{PAR} , the downward PAR irradiance, falls to 1% of its sub-surface value (Ryther, 1956). This convention is debatable (Banse, 2004). Although other slightly differing definitions exist, (as discussed in Morel & Gentili, 2004), E_{PAR} generally is the planar downward irradiance, over the 400–700 nm spectral domain (and expressed in $W\ m^{-2}$). Based on field determinations, purely empirical relationships between Z_{eu} and the average chlorophyll concentration within the euphotic layer, or the column chlorophyll content integrated over this layer, were previously established (Morel, 1988; Morel & Maritorena, 2001). More recently, Morel and Gentili (2004) presented the results of hyperspectral computations of the radiation transport based on the inherent optical properties of Case-1 waters. In particular, Z_{eu} was computed as a function of the near-surface concentration, $[Chl]_{surf}$, for various solar zenith angles (θ_s from 0° to 75°), and under two assumptions regarding the phytoplankton vertical profile. The first assumption is that of a uniform chlorophyll profile, which is typical of well-mixed waters. The second assumption accounts for the presence of a deep chlorophyll maximum (DCM), which is generally well developed in stratified oligotrophic waters. A gaussian shaped DCM is modeled as a function of $[Chl]_{surf}$ as in Morel and Berthon (1989) (whose results have been recently revisited and confirmed by Uitz et al., 2006). Fig. 9a shows the extreme Z_{eu} values (i.e., when θ_s is 0° or 75°) as a function of $[Chl]_{surf}$, and when the vertical pigment profiles is assumed to be uniform or structured (redrawn from Fig. 1 in Morel & Gentili, 2004). Fig. 9b presents recent field data in Case-1 waters encompassing a wide range of $[Chl]_{surf}$ and Z_{eu} values. They are all posterior to the data presented in Morel (1988, Fig. 1), and for all these new data, $[Chl]$ was determined via the HPLC technique (high performance liquid chromatography). Apart from those (within ellipses) described in the legend, the data are rather well organized along the theoretical curves (for $\theta_s = 45^\circ$). Interestingly, the best polynomial fit (data within the ellipses excluded) actually falls between the theoretical predictions for uniform or structured $[Chl]$ profiles. The scattering of these field data around the best fit corresponds to a mean average percent error of $\pm 14\%$. The SCAPA data (Fig. 9c), are more scattered (no screening), yet they confirm the trend already observed in Fig. 9b (the separate regression analysis of these data provides within their own uncertainty level the same relationship as indicated in the legend of Fig. 9b). Therefore the two datasets are merged, and the best polynomial fit as function of $X (= \log_{10}[Chl]_{surf})$, expresses as

$$\log_{10} Z_{eu} = 1.524 - 0.436 X - 0.0145 X^2 + 0.0186 X^3. \quad (10)$$

The frequency distribution of the ratio of the measured to the predicted Z_{eu} values is shown in inset. It is worth recalling that such an extrapolation of the near-surface information is valid for Case-1 waters only, and even in this case, extrapolating is not free from uncertainties (random natural variability is illustrated by Fig. 9b and c). The euphotic depth when Eq. (10) is applied to the $[Chl]_{surf}$ values of MODIS-A is mapped in Fig. 12b, with Z_{eu} ranging between 5 and 180 m.

4.2. Secchi disk depth

The prediction of the vertical visibility of a water column, commonly described by the depth where the Secchi disk disappears, is also considered a potentially useful by-product of the ocean color imagery, even if its true scientific contribution is rather limited. Historically, the Secchi disk procedure was valued by aquatic biologist as a simple index of the trophic activity, and a useful help when devising the strategy for in situ primary production experiments. Not surprisingly, the Secchi disk transparency maps are clearly related to those of $[Chl]$ as inferred from ocean color imagery (Lewis et al., 1988).

In the frame of remote sensing applications, the Secchi disk depth, denoted by Z_{sd} , bears, for similar reasons, the same kind of uncertainties that are attached to Z_{eu} . Indeed, Z_{sd} generally exceeds the thickness the layer seen by the sensor, so that its prediction presumes a certain homogeneity beyond this layer. Further, the visual measurement of Z_{sd} is also of polychromatic nature. It does not involve the 400–700 nm domain in a neutral fashion (as does PAR), but through a convolution with the photopic response of the “standard” human eye (CIE, 1931), which experiences a maximum around 555 nm, and is near zero at the two ends of the visible spectrum. Based on physical and physiological considerations, theory (Preisendorfer, 1986; Tyler, 1968) provides a useful formulation of Z_{sd}

$$Z_{sd} = \Gamma / [c_v(Z_{sd} \rightarrow 0) + K_{d,v}(0 \rightarrow Z_{sd})] \quad (11)$$

where the number Γ depends on the inherent initial contrast of the (white) disk against the surrounding water, and is also determined by the contrast detection threshold of the standard human observer. In the best viewing conditions (observer’s eyes below the water surface), a maximal Γ value would be about 8.7 (Tyler, 1968); more realistically, and for an observer above the water, Γ may be considerably lowered by the perturbing effects of the reflecting and wind roughened interface.

The coefficients c_v (beam attenuation coefficient) and $K_{d,v}$ (downward diffuse attenuation coefficient) are mean values for the upper layer of thickness Z_{sd} . They also are broad band coefficients, defined in reference to the photopic human vision (subscript v). More precisely, $K_{d,v}(0 \rightarrow Z_{sd})$ is the coefficient pertinent to the layer which extends from the surface down to Z_{sd} , and it deals with a photometric quantity, denoted by E_v , the downward illuminance. Illuminance is defined as being the convolution of the local $E_d(\lambda)$ with the photopic luminosity function, $\check{y}(\lambda)$, over the domain of this function (380–760 nm)

$$E_v(z) = \int E_d(\lambda, z) d\lambda = \int E_d(\lambda, z) \check{y}(\lambda) d\lambda. \quad (12)$$

Then $K_{d,v}(0 \rightarrow Z_{sd})$ is defined as

$$K_{d,v}(0 \rightarrow Z_{sd}) = (Z_{sd})^{-1} \ln [E_v(0)/E_v(Z_{sd})]. \quad (13)$$

To the extent that the Secchi disk albedo is spectrally neutral, such that the reflected light is uniformly proportional at all wavelengths to the incident light, the mean coefficient c_v for the ($Z_{sd} \rightarrow 0$) layer also involves the convolution of the spectral

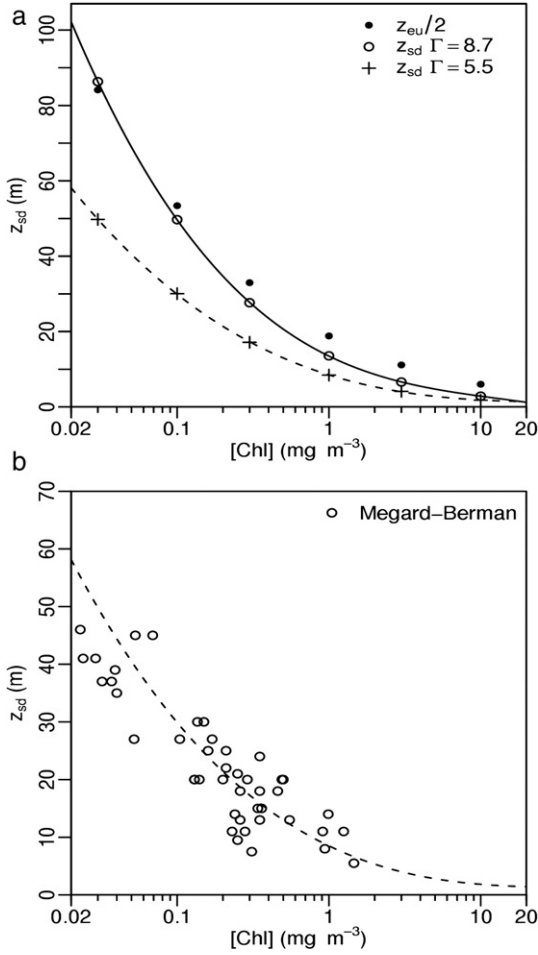


Fig. 10. a) As a function of $[Chl]$, depth of the mid-euphotic layer, ($Z_{eu}/2$) (black dots), and Secchi disk depth, Z_{sd} (circles), as computed through Eq. (15), with $\Gamma=8.7$, or computed according to Eq. (17), (dashed curve). b) Coincident observations (Megard and Berman, 1989) of Z_{sd} and $[Chl]$ in the Eastern Mediterranean Sea (pelagic stations), plotted for visual comparison with the curve redrawn from panel a, and for $\Gamma=5.5$.

beam attenuation coefficient, $c(\lambda)$, with the spectral distribution of illuminance at this depth Z_{sd} , according to

$$c_v(Z_{SD} \rightarrow 0) = (Z_{SD})^{-1} \ln \frac{\int E_v(\lambda, Z_{SD}) d\lambda}{\int E_v(\lambda, Z_{SD}) \exp(-c(\lambda)Z_{SD}) d\lambda}. \quad (14)$$

In Case-1 waters, $c(\lambda)$ and $K_d(\lambda)$, and thus $E_v(\lambda, Z)$, can be related to $[Chl]$ (e.g., Figs. 3 and A1 in Morel & Gentili, 2004); consequently, the above photopic quantities can also be produced as a function of $[Chl]$. The problem, however, is that the unknown Z_{sd} has to be estimated a priori before making use of the equations above. This is possible through an iterative process (see Appendix D). The resulting Z_{sd} values are plotted in Fig. 10a. The corresponding best fit, for $[Chl]$ between 0.02 and 20 mg m^{-3} , is expressed as:

$$(Z_{sd})_{8.7} = 13.5 - 19.6 X + 12.8 X^2 - 3.80 X^3 \quad (15)$$

where $X = \log_{10}[Chl]$ and the subscript 8.7 represents Γ .

Validation of the above approach is feasible through the use of the Secchi disk records which are stored in the United States National Oceanographic Data Center (US-NODC). This database includes 108 323 observations (from 1900 to 1991), the majority of which (66 009) are in the summer time (21 June to 21 September) and in the Northern hemisphere. These data can be compared to those computed via Eq. (15) from $[Chl]$ as retrieved from satellite imagery. A MODIS-A level 3 composite (spatial resolution 4.88 km) for the same summer time period (but for the year 2004 only) has been used for this comparison. When several Z_{sd} determinations coexisted within the same pixel, they were averaged; when the satellite $[Chl]$ was $> 15 \text{ mg m}^{-3}$, Z_{sd} was not computed (elimination of presumably coastal Case-2 waters). These averaging and selection procedures reduce the number of matchups to 30 531 (displayed on Fig. 11a). It appears that the modeled values, $Z_{sd, \text{mod}}$, generally exceed the measured values, $Z_{sd, \text{meas}}$. Some outliers (199) must be eliminated before performing the linear regression analysis. After this elimination, the analysis results in the following relationship:

$$Z_{sd, \text{mod}} = 1.238 + 1.572 Z_{sd, \text{meas}} \quad (r^2 = 0.62) \quad (16)$$

where the intercept (1.238 m) is negligible, and the slope (1.572) indicates the general bias. To account for the divergence between the modeled and measured values, the $\Gamma(8.7)$ coefficient is to be divided by this slope value, and becomes ~ 5.5 , that is probably a more realistic value on average for field observations from above

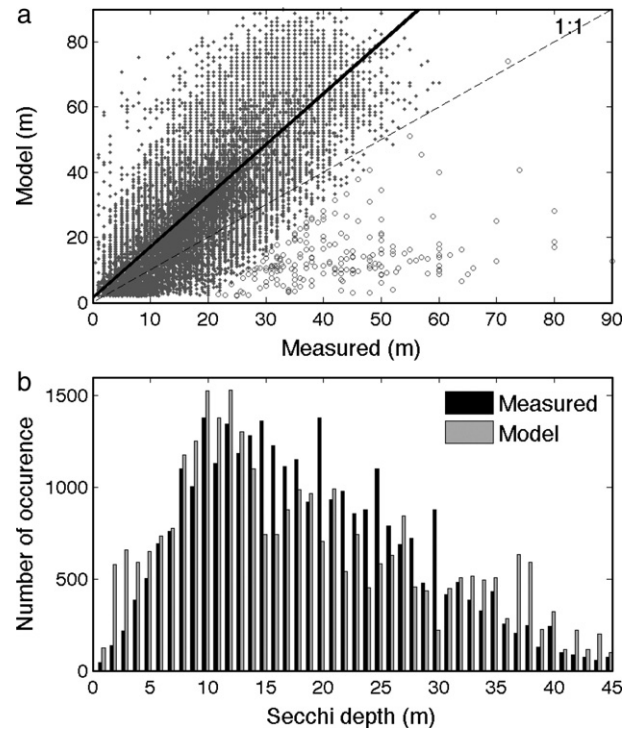


Fig. 11. a) Modeled Secchi disk depths, Z_{sd} , (Eq. (15) with $\Gamma=8.7$, and MODIS data) versus measured Z_{sd} (NODC). The crosses represent outliers eliminated from the regression analysis. The equation corresponding to the linear regression shown as a solid line is provided in the text (Eq. (16)). b) Histograms (1 m resolution) of the measured and computed Z_{sd} for the same dataset; the total number of data is 30332.

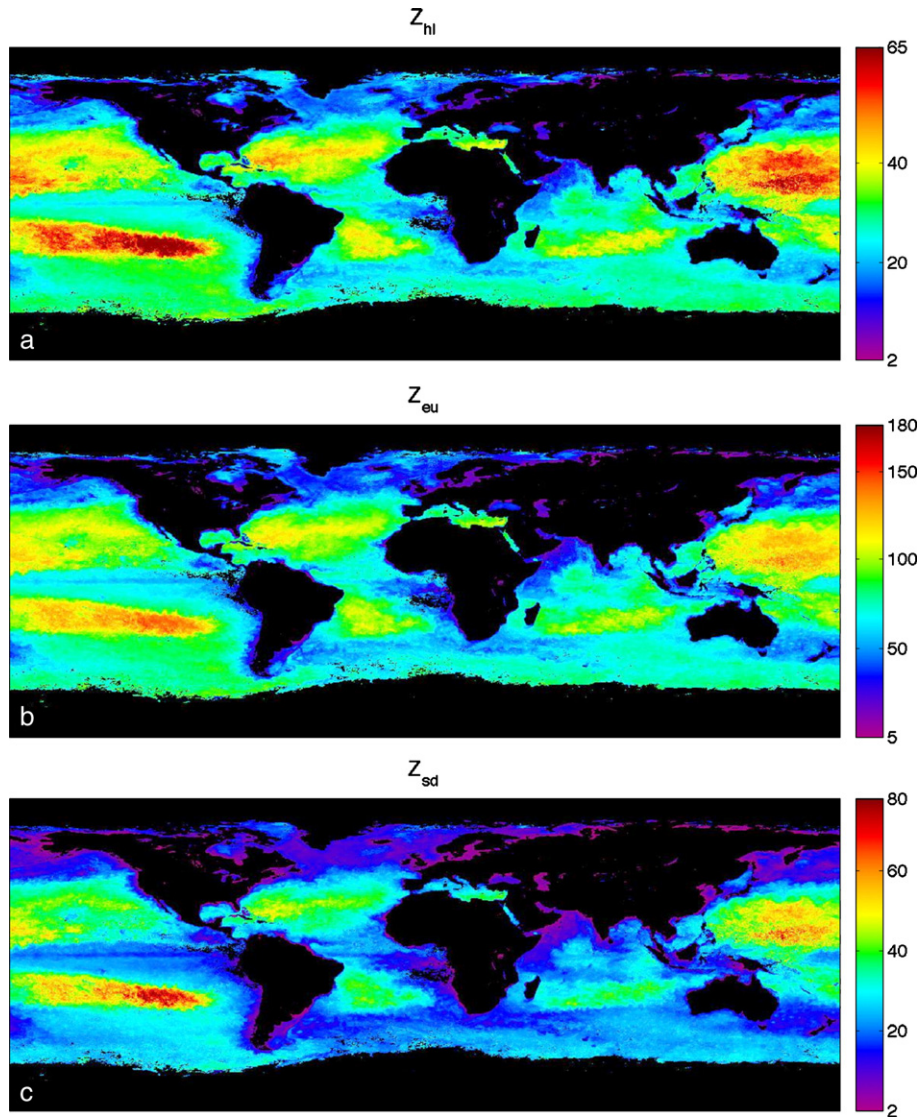


Fig. 12. Examples of applications, a) Thickness of the heated layer, Z_{hl} (between 2 and 65 m), as derived from $K_d(\text{PAR})_2$ via Eq. (9') applied to the MODIS composite and when [Chl] is obtained through OC3M-550, b) Depth of the euphotic layer (from 5 to 180 m) obtained via Eq. (10) applied to the SeaWiFS composite processed with OC4Me-555. c) Secchi disk depth (from 2 to 80 m) obtained via Eq. (17). Note that the linear color scales are identical but with differing end points.

the surface (Tyler, 1968). With this reduced Γ value, which leads to a thinner layer, Z_{sd} must be recomputed iteratively (Appendix D) and the resulting expression is

$$(Z_{sd})_{5,5} = 8.50 - 12.6X + 7.36X^2 - 1.43X^3 \quad (17)$$

(which actually is very close to Eq. (15) when multiplied by the ratio 5.5/8.7). At pelagic stations off Israel (depth >100 m), simultaneous measurements of [Chl] within the upper layer, and Z_{sd} , were carried out by Megard and Berman (1989). Despite some scatter and a reduced number of data (compared to those discussed below), they visually confirm (Fig. 10b) the validity of the above Eq. (17) (note that using $\Gamma=8.7$ would clearly provide an overestimate).

The observed Z_{sd} (NODC) and those computed (Eq. (17)) from the MODIS-A [Chl] Z_{sd} values are compared via a histogram analysis in Fig. 11b. The two histograms agree remarkably

well when considering the difference in time (months and years), the circulation variability, and uncontrolled artifacts, such as human and sensor fallibilities.

The cautions when using this approach must be emphasized. Firstly, the layer extending down to Z_{sd} is assumed to be homogeneous; inasmuch as [Chl] often increases with depth, the predicted value might overestimate the actual Z_{sd} depth. Secondly, the variability of the Γ parameter with viewing conditions directly impacts the reliability of any prediction. And thirdly, this tool can be used only in Case-1 waters, while the knowledge of Z_{sd} in coastal Case-2 waters, as visual index of water clarity, is desirable for various purposes (such as water quality monitoring, coastal management, and military purposes). More sophisticated approaches adapted to Case-2 waters optics are needed in such cases (Doron et al., 2007).

Because both Eqs. (10) and (17) make use of the same variable (i.e., $\log_{10}[\text{Chl}]$), the two depths, Z_{eu} and Z_{sd} are

algebraically related, independently of the underlying physics and possible heterogeneities within the water column. Such numerical relationships, plausible within, but constrained by, the hypotheses for Case-1 waters, have not been tested against field determinations. The Z_{eu} – Z_{sd} relationship, recurrently sought for by biologists, would be:

$$Z_{eu} = 5.61 + 4.04 Z_{sd} - 0.033 Z_{sd}^2. \quad (18)$$

The map of Z_{sd} (Fig. 12c), obviously exhibits the same patterns as in Fig. 12b, yet with a shifted scale, between 2 and 65 m (instead of 5–180 m for Z_{eu}).

5. Conclusions and perspectives

The present study was restricted to the examination of divergences resulting only from the use of differing algorithms for the retrieval of [Chl] and K_d . Indeed, the same initial marine signals (radiance or reflectance) have been successively introduced into the various algorithms for a comparison of the outputs. As stressed at the beginning, differences in the products as delivered by space agencies may differ for other reasons (signal calibration at the top of atmosphere, atmospheric correction schemes), which were not examined here. One part of the differences in the final products, however, originates only from the marine algorithm diversity, and it is essential to quantify separately the magnitude of this impact.

With respect to the [Chl] retrieval, the algorithms presently in use are not totally coincident, particularly in the domain of low concentration. There is presently no decisive argument, however, to select one algorithm over another one among those available. The empirical algorithms developed for SeaWiFS and MODIS-A are based on the same R_{rs} vs [Chl] dataset (basically NOMAD and posterior data); they also have been adjusted to make them as compatible as possible. The semi-analytical algorithm developed for MERIS also involves field data (for K_d vs [Chl]), but this dataset is completely independent from the NOMAD database. It is extremely reassuring that these two differing approaches (as well as the two datasets) lead to convergent results, at least over most of the [Chl] range.

In the future perspective of merging data from various sensors, however, the divergence of the returns at the extreme ends of the [Chl] range may pose a problem. Using specific algorithms tuned for each sensor (i.e., for each band setting), but all deriving from the same hyperspectral bio-optical model is probably a convenient tool to get a sensor-independent product. Along this line, the set of OC4Me, OC4Me555, and OC3Me550 algorithms would satisfy this requirement. Such a choice, however, can always be contested, but less disputable is the resulting consistency. Actually, and if another choice is made, the reversibility is always possible and easy. Indeed, the relationships graphically displayed in Fig. 2b are pivotal (5th order polynomials in both directions available on request), for they allow inter-convertibility and easy reversibility of the [Chl] products.

With respect to the $K_d(490)$ coefficient, and its immediate derivative (the $K(\text{PAR})$ coefficient), a unified solution is also desirable. The historical approach based on a ratio of remote sensing reflectances implies that several algorithms are specifically developed for each sensor (and band setting), which in turn implies that enough data are available for the specific wavelengths 550, 555, and 560 nm. Assuming that such a requirement is fulfilled, the application of a more realistic curvilinear algorithm (of the OK2 type) is preferable to the use of purely empirical (linear) expressions which induce systematic errors. The use of [Chl] as an intermediate link is another solution (actually is a solution close to that offered by OK2), which presents the advantage of ensuring an overall consistency between the sensors products (once the [Chl] differences are resolved). The validity of this approach is reinforced by the coincidence of the two datasets (NOMAD and LOV), which allows their merging and the production of a highly significant relationship between $K_d(490)$ and [Chl]. Another benefit lies in the fact that K_d coefficients at wavelengths other than 490 nm (Table 4), as well as $K(\text{PAR})$, can be produced in the same way. The applicability of such methods, however, is restricted to Case-1 waters only; for more complex waters and higher K_d values, other approaches (e.g. Lee et al., 2005) must be envisaged.

Those products which can also be derived from the chlorophyll concentration (in Case-1 waters), such as the thickness of the solar heated layer, the euphotic depth, and the Secchi disk depth, could be produced at the level of individual sensors, or as well by using the merged [Chl] products of these sensors. In addition to natural

Table 4

Empirical relationships of the form $K_d(\lambda) = K_w(\lambda) + \chi(\lambda) [\text{Chl}]^{e(\lambda)}$, for various wavelengths, and associated statistics

Wavelength (nm) and K_w (m^{-1})	LOV dataset	Merged dataset (LOV+NOMAD)
412 $K_w=0.007932$	$\chi=0.13328$ $e=0.61990$ RMSE=0.121 $R^2=0.957$ Bias=−0.00469	$\chi=0.12994$ $e=0.63594$ RMSE=0.141 $R^2=0.902$ Bias=−0.00447
443 $K_w=0.00948$	$\chi=0.11710$ $e=0.64386$ RMSE=0.104 $R^2=0.997$ Bias=−0.00622	$\chi=0.11261$ $e=0.66144$ RMSE=0.127 $R^2=0.934$ Bias=−0.00573
490 $K_w=0.0166$	$\chi=0.082530$ $e=0.62588$ RMSE=0.0920 $R^2=0.983$ Bias=−0.00605	$\chi=0.077298$ $e=0.67155$ RMSE=0.118 $R^2=0.930$ Bias=−0.0106
510 $K_w=0.03385$	$\chi=0.068490$ $e=0.62611$ RMSE=0.0791 $R^2=0.987$ Bias=−0.00796	$\chi=0.063145$ $e=0.65619$ RMSE=0.0949 $R^2=0.908$ Bias=−0.0125
555 $K_w=0.06053$	$\chi=0.056050$ $e=0.50073$ RMSE=0.0646 $R^2=0.909$ Bias=−0.00775	$\chi=0.050234$ $e=0.50958$ RMSE=0.0734 $R^2=0.763$ Bias=−0.0116

The data with $K_d < K_w$ have been discarded before performing the regression analysis on the log transform of the quantities $(K_d - K_w) = K_{\text{bio}}$, and [Chl].

variability, the predictive capabilities of the algorithms providing these quantities are limited by the uncertainties linked to the assumptions needed for the downward extrapolations.

Other products, such as the total suspended matter content, the dissolved/detrital colored matter concentration, or some inherent optical properties are also of biogeochemical interest. For these parameters, however, strong differences in the methods by which they are derived (IOCCG, 2006) presently impede a meaningful merging until a consensus can be reached.

The exactly normalized radiances, $nLw(\lambda)$, are the primary and well defined marine products to be firstly considered as candidates for the merging process. Because of the differing spectral bands, such a process requires the use of transfer functions (not detailed here), which can be straightforwardly obtained via the hyperspectral model (this is particularly needed for the green channels at 550, 555, and 560 nm of MODIS-A, SeaWiFS, and MERIS, respectively). Using the various $nLw(\lambda)$ radiances regardless of their spectral position, is another solution (as recommended by Maritorena & Siegel, 2005). In such a case, a model-based method (GSM01, Maritorena et al., 2002) able to cope with, and to take advantage of, the differing wavelengths, allows by inversion the simultaneous derivation of geophysical products such as [Chl] and inherent optical properties (namely the backscattering coefficient and the absorption coefficient at 443 nm by colored dissolved and detrital materials). This approach should advantageously be developed in parallel with a “classical” method, which simply consists of directly merging the geophysical products as they are provided by space agencies.

Acknowledgements

We thank three anonymous reviewers for their constructive comments. Very helpful and detailed suggestions by one of them have considerably improved the first version of this paper.

Appendix A. List of acronyms and abbreviations

Agencies and organizations

ESA	European Space Agency
IOCCG	International Ocean Colour Coordinating Group
NASA	National Aeronautics and Space Administration
NODC	(US) National Oceanographic Data Center
SIMBIOS	Sensor Intercomparison and Merger for Biological and Interdisciplinary Ocean Studies

Instruments and algorithms

CZCS	Coastal Zone Color Scanner
MERIS	Medium Resolution Imaging Spectrometer
MODIS-A	Moderate Resolution Imaging Spectroradiometer-Aqua
SeaWiFS	Sea-viewing Wide Field-of-view Sensor
OCy-xxx	Ocean Chlorophyll algorithms (y =number of spectral bands, 2, 3, 4; xxx=green wavelength, 550, 555, or 560 nm)
OK2-xxx	Ocean K_d algorithms (2 spectral bands)

Quantities

PAR	Photosynthetically Available Radiation
Z_{eu}	Depth of the bottom of the euphotic layer
Z_{hl}	Depth of the heated layer (95% of solar heat deposition)
Z_{sd}	Secchi disk depth

Appendix B

Definitions and relationships (the wavelength dependency is omitted, as well as dependencies on wind speed and aerosol optical thickness)

Quantities	(units)	Definition
<i>Irradiance (reflectance) ratio</i>	(dimensionless)	$R = E_u(0^-) / E_d(0^-)$ $E_u(0^-)$ and $E_d(0^-)$ are the upward and downward irradiance <i>beneath</i> the surface (at null depth, symbol 0^-).
$E_d(0^-) = t_{aw} E_d(0^+)$, where $E_d(0^+)$ is the downward irradiance <i>above</i> the surface (symbol 0^+), and t_{aw} is the interface transmittance (from air to water) for irradiance from sky and sun, and thus depends chiefly on the solar zenith angle (θ_s). In particular for this reason (but not exclusively), R depends on illumination conditions. It is convenient to define R_0 , the value of R when the sun is at zenith (Fig. 7 in Morel et al., 2002).		
<i>Remote sensing reflectance</i>	(sr^{-1})	$R_{rs} = L_w(0^+) / E_d(0^+)$ $E_d(0^+)$ is the downward irradiance (as above); $L_w(0^+)$, actually to be written as $L_w(\theta_v, \theta_s, \varphi, 0^+)$, is the water-leaving radiance, which depends on the geometry of observation, namely on the viewing angle (θ_v), the solar zenith angle (θ_s), and the azimuth difference (φ) between the solar plane and the plane of observation. $L_w(0^+)$ is related to $L_u(0^-)$, the in-water upward radiance, through $L_w(0^+, \theta_v, \theta_s, \varphi) = L_u(0^-, \theta'_v, \theta'_s, \varphi_s) (t_{wa} / n^2)$, where θ'_v and θ'_s and θ'_s are related through Snell's law, t_{wa} is the interface upward (water to air) transmittance (for the θ'_v direction) and n is the refractive index of seawater.
<i>Normalized water-leaving radiance</i>	($W m^{-2} sr^{-1}$)	$nLw = F_0 [L_w(0^+) / E_d(0^+)]$ $= F_0 R_{rs}$ where F_0 is the extra-terrestrial solar irradiance, at mean Sun–Earth distance.
<i>Q-factor</i>	(sr)	$Q(\theta'_v, \theta_s, \varphi) = E_u(0^-, \theta_s) / L_u(0^-, \theta'_v, \theta'_s, \varphi)$ Is the ratio of the upward irradiance to any upward radiance, both beneath the surface, and depends on the geometry.

B.1. Relationships

In the processing made by the Space Agencies, the above quantities, nLw , R_{rs} (or $\rho_w = \pi R_{rs}$, for MERIS) are corrected for the bi-directional effects (via the “ f/Q correction”, Eq. (13.20) in Morel & Mueller, 2002). These exactly normalized quantities (superscript “ex”) are related to the irradiance ratio, R_0 (i.e., the R value when $\theta_s = 0$), through

$$R_{rs}^{ex} = R_0 (\mathfrak{R}_0 / Q_0) \quad (B - 1)$$

and

$$nLw^{ex} = R_0 (\mathfrak{R}_0 / Q_0) F_0 \quad (B - 2)$$

where

$$R_0 = R[f_0(\theta_s = 0) / f(\theta_s)]. \quad (B - 3)$$

Q_0 is the particular Q -value when L_u is the radiance originating from nadir ($\theta'_v = \theta_v = 0$), and when the sun is at zenith ($\theta_s = 0$). This quantity Q_0 depends slightly on the wavelength (λ), and more importantly on the inherent optical properties (IOP) of the water body, and thus upon [Chl] (see Fig. 13.7a, in the above reference). The dimensionless factor \mathfrak{R} merges the effect of reflection and refraction (Gordon, 2005; Wang, 2006), and \mathfrak{R}_0 (~ 0.529) is the particular \mathfrak{R} value when the geometrical

conditions are as above (sun at zenith, and a nadir viewing angle). In practice, \mathfrak{R}_0 is spectrally neutral and independent from the water body. The fraction $[f_0(\theta_s=0)/f(\theta_s)]$ depends slightly on θ_s and IOP (thus on λ and $[\text{Chl}]$).

For SeaWiFS and MODIS, the empirical retrieval of $[\text{Chl}]$ is made by using ratios of R_{rs} , whereas the retrieval of $K_d(490)$ is made by using an nLw ratio (Eq. (7)). The MERIS semi-analytical algorithm for $[\text{Chl}]$ is based on ratios of R_0 . This means that these ratios are not strictly equivalent. According to Eqs. (B-1) and (B-2), and by considering that \mathfrak{R}_0 is not wavelength-dependent, the ratios for two wavelengths λ_i and λ_j of R_{rs} and nLw are related to the R ratios according to

$$R_{rs}^{\text{ex}}(\lambda_i)/R_{rs}^{\text{ex}}(\lambda_j) = [R_0(\lambda_i)/R_0(\lambda_j)][Q_0(\lambda_j)/Q_0(\lambda_i)] \quad (\text{B} - 4)$$

and

$$\text{nLw}^{\text{ex}}(\lambda_i)/\text{nLw}^{\text{ex}}(\lambda_j) = [R_0(\lambda_i)/R_0(\lambda_j)][Q_0(\lambda_j)/Q_0(\lambda_i)][F_0(\lambda_i)/F_0(\lambda_j)]. \quad (\text{B} - 5)$$

For a given $(\lambda_j - \lambda_i)$ couple, the $[F_0(\lambda_i)/F_0(\lambda_j)]$ ratio is a constant. In contrast, the $[Q_0(\lambda_j)/Q_0(\lambda_i)]$ ratios differ slightly from unity and depend on $[\text{Chl}]$ (see Fig. 13.7a in Morel & Mueller, 2002); the maximal deviation (4%) is observed at low $[\text{Chl}]$ (0.03 mg m^{-3}), where $Q_0(560)/Q_0(443)=0.96$. These small variations have nevertheless to be accounted for when comparing the algorithms.

Appendix C. Datasets used in the present study

The NOMAD (NASA bio-Optical Marine Algorithm Data) publicly available dataset is described by Werdell and Bailey (2005). It contains simultaneous algal pigment concentration and various radiometric observations; in particular, it includes the remote sensing reflectance and diffuse attenuation coefficients at specific wavelengths, in correspondence with those of several ocean color sensors. The NOMAD data used in the present study are only those with $[\text{Chl}]$ determinations made via HPLC.

The LOV (Laboratoire d'Océanographie de Villefranche) dataset includes hyperspectral planar (upward and downward) irradiance determinations at various depths, from which spectral irradiance reflectance and diffuse attenuation coefficients are derived. The data acquisition started in 1970 (SCOR-WG15 Discoverer cruise). The present data bank originally rests on the data used in Morel (1988), and in Morel and Maritorena (2001), to which new data have been added, namely from the following cruises: PROSOPE (1999, Moroccan upwelling and Mediterranean Sea), BENCAL (2002, Benguela Current), AOPEX (2004, Mediterranean Sea), and BIOSOPE (2004, Eastern South Pacific). For all these new data, $[\text{Chl}]$ was determined by high performance liquid chromatography (HPLC). The instruments and methods are described in Barlow et al. (2003) and Morel et al. (2006, 2007) (see also http://www.obs-vlfr.fr/proof/index_vt.htm). Before 1991, $[\text{Chl}]$ was determined by spectrophotometry; starting with EUMELI cruises (1992–1993), $[\text{Chl}]$ was exclusively determined via HPLC method.

The SCAPA archive (Self-Consistent AOP Profiles Archive; S.B. Hooker) was created from an extensive set of field campaigns

throughout the world ocean (McClain et al., 2004), primarily (albeit not exclusively) in Case-1 waters. The free-fall multi-channel sensor profilers (measuring upward radiance and irradiance, and downward irradiance) were operated according to strategies (Hooker & Maritorena, 2000) which are in strict adherence to the Ocean Optics Protocols (Mueller, 2003); this includes a rigorous quality control of the data (acquisition and processing), and a set of quality assurance procedures during the sensor calibration. The radiometric calibration facilities are traceable to the National Institute of Standards and Technology (Hooker et al., 2002). The $[\text{Chl}]$ was determined via HPLC in a small number of laboratories whose capabilities have been established in international round robins to be within 10% (Hooker et al., 2005).

Appendix D. Iterative estimate of the Secchi disk depth

To initialize the iterative process leading to the estimate of Z_{sd} , the first step consists of adopting $Z_{10\%}$, the depth where PAR is reduced to 10% of its surface value, which is known to be roughly of the same order as Z_{sd} . By approximation, $Z_{10\%}$ for varying $[\text{Chl}]$ is taken as being $Z_{eu}/2$ for a uniform $[\text{Chl}]$ profile and for a sun angle equal to 30° (Table 2 in Morel & Gentili, 2004). Then the spectral Eq. (12) is used to compute the downward illuminance E_v above the surface and at $Z_{eu}/2$. The appropriate photopic K_{dv} and c_v coefficients are obtained through Eqs. (13) and (14); they allow a first estimate of Z_{sd} for the various $[\text{Chl}]$ to be obtained via Eq. (11) (calculated with $\Gamma=8.7$). The same computations (K_{dv} and c_v) are repeated with this first depth estimate, leading to a second estimate of Z_{sd} (a third iteration is ineffective). Note also that the use of a starting point other than $Z_{eu}/2$ has no effect on the final results, but may increase the number of needed iterations. The initial $Z_{eu}/2$ values, as well as the final Z_{sd} values, are displayed on Fig. 11a. In low $[\text{Chl}]$ and blue waters, Z_{sd} exceeds slightly $Z_{10\%}$, whereas the converse holds true in waters with higher $[\text{Chl}]$; this a logical consequence of the increase in the ratio K_{dv}/c_v with increasing $[\text{Chl}]$ (see Eq. (8) in Tyler, 1968). An old rule of thumb often used by biologists, “the Secchi disk depth approximately provides the 10% light level ($Z_{eu}/2$), is not far off, were $\Gamma=8.7$. When another Γ value is adopted (e.g., 5.5), the same iterative scheme is also operated. As the Z_{sd} depth is lesser in this case, its determination requires three successive iterations if the starting point is the $Z_{eu}/2$ depth, and the resulting Z_{sd} value is considerably smaller than $Z_{eu}/2$.

References

- Antoine, D., Morel, A., Gordon, H. R., Banzon, V. F., & Evans, R. H. (2005). Bridging ocean color observations of the 1980s and 2000s in search of long-term trends. *Journal of Geophysical Research*, 110. doi:10.1029/2004JC002620
- Austin, R. W., & Petzold, T. J. (1981). The determination of the diffuse attenuation coefficient of sea water using the coastal zone color scanner. In J. F. R. Gower (Ed.), *Oceanography from space* (pp. 239–256). New York: Plenum Press.
- Austin, R. W., & Petzold, T. J. (1986). Spectral dependence of the diffuse attenuation coefficient of light in ocean waters. *Optical Engineering*, 25, 471–479.
- Baker, K. S., & Smith, R. C. (1982). Bio-optical classification and model of natural waters. *Limnology and Oceanography*, 27, 500–509.

- Banase, K. (2004). Should we continue to use the 1% light depth for estimating the compensation depth of phytoplankton for another 70 years? *Limnology and Oceanography Bulletin*, 13, 49–51.
- Barlow, R., Sessions, H., Silulwane, N., Engel, H., Hooker, S. B., et al. (2003). BENCAL cruise report. *NASA-Technical Memo*, 27, 1–84.
- Bricaud, A., Morel, A., Babin, M., Allali, K., & Claustre, H. (1998). Variations of light absorption by suspended particles with chlorophyll a concentration in oceanic (Case 1) waters: Analysis and implications for bio-optical models. *Journal of Geophysical Research*, 103, 31033–31044.
- Campbell, J. (2004). Issues linked to the use of binned data in models: An example using primary production. In V. Stuart (Ed.), *Guide to the creation and use of ocean colour, level-3, binned data products, report number 4. Reports of the International Ocean-Colour Coordinating Group* (pp. 47–57). Dartmouth: IOCCG.
- Carr, M. -E., Friedrichs, M. A. M., Schmeltz, M., Aité, M. N., Antoine, D., Arrigo, K. R., et al. (2006). A comparison of global estimates of marine primary production from ocean color. *Deep-Sea Research II*, 53, 741–770.
- C.I.E. (1931). *Proceedings 1931(Commission Internationale de l'Eclairage)*. Cambridge: Cambridge University Press.
- Clark, D. K. (1981). Phytoplankton algorithms for the NIMBUS-7 CZCS. In J. F. R. Gower (Ed.), *Oceanography from space* (pp. 227–238). New York: Plenum.
- Claustre, H., Morel, A., Hooker, S. B., Babin, M., Antoine, D., Oubelkheir, K., et al. (2002). Is desert dust making oligotrophic waters greener? *Geophysical Research Letters*, 29(10). doi:10.1029/2001GL014056
- Doron, M., Babin, M., Mangin, A., Fanton d' Andon, O. (2007). Estimation of light penetration, and horizontal and vertical visibility in oceanic and coastal waters from surface reflectance. *Journal of Geophysical Research*, 112. doi:10.1029/2006JC004007
- Gordon, H. R. (2005). Normalized water-leaving radiance: Revisiting the influence of surface roughness. *Applied Optics*, 44, 241–248.
- Gordon, H. R., Brown, O. B., Ewans, R. H., Brown, J. W., Smith, R. C., Baker, K. S., et al. (1988). A semi-analytical radiance model of ocean color. *Journal of Geophysical Research*, 93, 10909–10924.
- Gordon, H. R., Brown, O. B., & Jacobs, M. M. (1975). Computed relations between inherent and apparent optical properties of a flat homogeneous ocean. *Applied Optics*, 14, 417–427.
- Gordon, H. R., & McCluney, W. R. (1975). Estimation of the depth of sunlight penetration in the sea for remote sensing. *Applied Optics*, 14, 413–416.
- Gordon, H. R., & Morel, A. (1983). *Remote assessment of ocean color for interpretation of satellite visible imagery: A review, Vol. 114*. New York: Springer-Verlag.
- Hooker, S. B., & Maritorena, S. (2000). An evaluation of oceanographic radiometers and deployment methodologies. *Journal of Atmospheric and Oceanic Technology*, 17, 811–830.
- Hooker, S. B., McClain, C. R., Firestone, E. R., Westphal, T. L., Yeh, E. N., & Geo, Y. (1994). The SeaWiFS Bio-optical Archive and Storage System (SeaBASS), Part 1. *NASA Technical Memo*, 104566, 20, 37.
- Hooker, S. B., McLean, S., Sherman, J., Small, M., Lazin, G., Zibordi, G., et al. (2002). The seventh SeaWiFS intercalibration round-robin experiment (SIRREX_7, March 1999). *Nasa Technical Memo*, 2002-206892, 17, 1–69.
- Hooker, S. B., Van Heukelem, L., Thomas, C. S., Claustre, H., Ras, J., Schlüter, L., et al. (2005). The second SeaWiFS HPLC analysis round robin experiment. *NASA Tech. Memo*, 2005-212785, 112.
- IOCCG (2000). Remote sensing of ocean colour in coastal, and other optically-complex, waters, report number 3. In V. Stuart (Ed.), *Reports of the International Ocean-Colour Coordinating Group* (pp. 1–139). Dartmouth, Canada: Nova Scotia.
- IOCCG (2004). Guide to the creation and use of ocean colour, level-3, binned data products, report number 4. In V. Stuart (Ed.), *Reports of the International Ocean-Colour Coordinating Group* (pp. 1–88). Dartmouth, Canada: Nova Scotia.
- IOCCG (2006). Remote sensing of inherent optical properties: Fundamentals, tests of algorithms and applications. Report number 5. In V. Stuart (Ed.), *Reports of the International Ocean-Colour Coordinating Group* (pp. 1–126). Dartmouth, Canada: Nova Scotia.
- Lee, Z. P., Carder, K. L., & Arnone, R. (2002). Deriving inherent optical properties from water color: A multi-band quasi-analytical algorithm for optically deep waters. *Applied Optics*, 41, 5755–5772.
- Lee, Z. P., Darecki, M., Carder, K. L., Davis, C., Stramski, D., & Rhea, W. J. (2005). Diffuse attenuation coefficient of downwelling irradiance: An evaluation of remote sensing methods. *Journal of Geophysical Research*, 110. doi:10.1029/2004JC002573
- Lewis, M. R., Kuring, N., & Yentsch, C. (1988). Global patterns of ocean transparency: Implication for the new production of open ocean. *Journal of Geophysical Research*, 93, 6847–6856.
- Loisel, H., & Morel, A. (1998). Light scattering and chlorophyll concentration in Case 1 waters: A reexamination. *Limnology and Oceanography*, 43, 847–858.
- Loisel, H., Nicolas, J. M., Deschamps, P. Y., & Frouin, R. (2002). Seasonal and inter-annual variability of the particulate matter in the global ocean. *Geophysical Research Letters*, 29, 2196. doi:10.1029/2002GL015948
- Maritorena, S., & Siegel, D. A. (2005). Consistent merging of satellite ocean color data sets using a bio-optical model. *Remote Sensing of Environment*, 94, 429–440.
- Maritorena, S., Siegel, D. A., & Peterson, A. (2002). Optimization of a semi-analytical ocean color model for global applications. *Applied Optics*, 41, 2705–2714.
- McClain, C. R., Feldman, G. C., & Hooker, S. B. (2004). An overview of the SeaWiFS strategies for producing a climate research quality global ocean bio-optical time series. *Deep-Sea Res II*, 51, 5–42.
- Megard, R. O., & Berman, T. (1989). Effects of algae on the Secchi transparency of the southeastern Mediterranean Sea. *Limnology and Oceanography*, 34, 1640–1655.
- MERIS (2007). Algorithm theoretical basis document 2.9: Pigment index retrieval in Case 1 waters. <http://envisat.esa.int/instruments/meris/pdf/>
- Morel, A. (1974). Optical properties of pure water and pure seawater. In N. G. J. E. Steeman-Nielsen (Ed.), *Optical aspects of oceanography* (pp. 1–24). San Diego: Academic.
- Morel, A. (1988). Optical modeling of the upper ocean in relation to its biogenous matter content. *Journal of Geophysical Research*, 93, 10749–10768.
- Morel, A. (1997). Consequences of a *Synechococcus* bloom upon the optical properties of oceanic (Case 1) waters. *Limnology and Oceanography*, 42, 1746–1754.
- Morel, A., Antoine, D., & Gentili, B. (2002). Bidirectional reflectance of oceanic waters: Accounting for Raman emission and varying particle scattering phase function. *Applied Optics*, 41, 6289–6306.
- Morel, A., & Berthon, J. -F. (1989). Surface pigments, algal biomass profiles, and potential production of the euphotic layer: Relationships reinvestigated in view of remote sensing applications. *Limnology and Oceanography*, 34, 1545–1562.
- Morel, A., & Gentili, B. (1996). Diffuse reflectance of oceanic waters III: Implication of bidirectionality for the remote sensing problem. *Applied Optics*, 35, 4850–4862.
- Morel, A., & Gentili, B. (2004). Radiation transport within oceanic (Case 1) water. *Journal of Geophysical Research*, 109. doi:10.1029/2003JC002259
- Morel, A., Gentili, B., Chami, M., & Ras, J. (2006). Bio-optical properties of high chlorophyll Case 1 waters, and of yellow substance-dominated Case 2 waters. *Deep-Sea Res I*, 53, 1439–1459.
- Morel, A., Gentili, B., Claustre, H., Babin, M., Bricaud, A., Ras, J., et al. (2007). Optical properties of the “clearest” waters. *Limnology and Oceanography*, 52, 217–229.
- Morel, A., & Gordon, H. R. (1980). Report of the working group on water color. *Boundary Layer Meteorology*, 18, 343–355.
- Morel, A., & Maritorena, S. (2001). Bio-optical properties of oceanic waters: A reappraisal. *Journal of Geophysical Research*, 106, 7163–7180.
- Morel, A., & Mueller, J. L. (2002). Normalized water-leaving radiance and remote sensing reflectance: Bidirectional reflectance and other factors. *Ocean optics protocols for satellite ocean color sensor validation, NASA/TM-2002-210004/Rev3-Vol. 2* (pp. 183–210).
- Morel, A., & Prieur, L. (1977). Analysis of variations in ocean color. *Limnology and Oceanography*, 22, 709–722.
- Mueller, J. L. (2000). SeaWiFS algorithm for the diffuse attenuation coefficient, K_d(490) using water-leaving radiance at 490 and 555 nm. *SeaWiFS postlaunch technical report series, Vol. 11* (pp. 24–27) (Part 3).
- Mueller, J. L. (2003). Radiometric measurements and data analysis protocols. *NASA Technical Memo*, 2003-21621, Rev. 4 Vol. III. 1–20.

- O'Reilly, J. E., Maritorena, S., Mitchell, B. G., Siegel, D. A., Carder, K. L., Garver, S. A., et al. (1998). Ocean color algorithms for SeaWiFS. *Journal of Geophysical Research*, 103, 24937–24953.
- O'Reilly, J. E., Maritorena, S., Siegel, D. A., O'Brien, M. C., Toole, D., Mitchell, B. G., et al. (2000). Ocean color chlorophyll a algorithms for SeaWiFS, OC2, and OC4: version 4. *SeaWiFS postlaunch calibration and validation analyses, Part 3, NASA/TM 206892, Vol. 11* (pp. 9–23).
- Pope, R. M., & Fry, E. S. (1997). Absorption spectrum (380–700 nm) of pure water. II. Integrating cavity measurements. *Applied Optics*, 36, 8710–8723.
- Preisendorfer, R. W. (1986). Secchi disk science: Visual optics of natural waters. *Limnology and Oceanography*, 31, 909–926.
- Rochford, P. A., Birol-Kara, A., Wallecraft, A. J., & Arnone, R. A. (2001). Importance of solar subsurface heating in ocean general circulation models. *Journal of Geophysical Research*, 106, 30923–30938.
- Ryther, J. H. (1956). Photosynthesis in the ocean as a function of light intensity. *Limnology and Oceanography*, 1, 61–70.
- SIMBIOS (1999). SIMBIOS Project 1998 Annual Report. *NASA/TM-1999-208645* (pp. 1–105).
- Smith, R. C., & Baker, K. S. (1981). Optical properties of the clearest natural waters (200–800 nm). *Applied Optics*, 20, 177–184.
- Tyler, J. E. (1966). Report on the second meeting of the Joint Group of experts on photosynthetic radiant energy. *UNESCO Technical Papers in Marine Science, Vol. 5* (pp. 1–11).
- Tyler, J. E. (1968). The Secchi disk. *Limnology and Oceanography*, 13, 1–6.
- Uitz, J., Claustre, H., Morel, A., & Hooker, S. B. (2006). Vertical distribution of phytoplankton communities in open ocean: An assessment based on surface chlorophyll. *Journal of Geophysical Research*, 111, C08005. doi:10.1029/2005JC003207
- Wang, M. (2006). Effects of ocean surface reflectance variation with solar elevation on normalized water-leaving radiance. *Applied Optics*, 45, 4122–4128.
- Wang, M., Knobelspiesse, K. D., & McClain, C. R. (2005). Study of the Sea-Viewing Wide Field-of-view Sensor (SeaWiFS) aerosol optical property data over ocean in combination with the ocean color products. *Journal of Geophysical Research*, 110, D10S06. doi:10.1029/2004JD004950
- Werdell, P. J. (2005). OceanColor K490 algorithm evaluation. http://oceancolor.gsfc.nasa.gov/REPROCESSING/SeaWiFS/R5.1/k490_update.html
- Werdell, P. J., & Bailey, S. W. (2002). *The SeaWiFS Bio-optical Archive and Storage System (SeaBASS): Current architecture and implementation* (pp. 1–45).
- Werdell, P. J., & Bailey, S. W. (2005). An improved in-situ bio-optical data set for ocean color algorithm development and satellite data product validation. *Remote Sensing of Environment*, 98, 122–140.
- Woods, J. D., Barkman, W., & Horch, A. (1984). Solar heating of the oceans, diurnal, seasonal and meridional variation. *Quarterly Journal of the Royal Meteorological Society*, 110, 633–656.
- Zaneveld, J. R., Kitchen, J. C., & Mueller, J. L. (1993). Vertical structure of productivity and its vertical integration as derived from remotely sensed observations. *Limnology and Oceanography*, 38, 1384–1393.